Revision 2

Mineralogical characterization of individual growth structures of Mn-nodules with different Ni+Cu content from the central Pacific Ocean

Anna V. Wegorzewski[1]*, Thomas Kuhn[1], Reiner Dohrmann[1,2], Richert Wirth[3], Sylvain Grangeon[4]

[1]Federal Institute for Geosciences and Natural Resources (BGR), Stilleweg 2, D-30655 Hannover, Germany

* Corresponding author: email, anna.wegorzewski@bgr.de

[2]State Authority of Mining, Energy and Geology (LBEG), Stilleweg 2, D-30655 Hannover, Germany

[3]Helmholtz Centre Potsdam, German Research Centre for Geosciences (GFZ), Telegrafenberg, Buiding C, 14473 Potsdam, Germany

[4]BRGM, 3 Avenue Claude Guillemin, 45060 Orléans cedex2, France

Abstract

The mineralogy of manganese nodules from the German license area in the eastern Clarion and Clipperton Zone (CCZ) of the central Pacific Ocean was studied using X-ray diffraction. Their individual nm to µm thick genetic different (hydrogenetic/diagenetic) layer growth structures were investigated using high-resolution transmission electron microscopy. Relationships between the mineral phases and metal content (e.g., Ni+Cu) were assessed with electron microprobe analyzer.

The main manganese phase detected in nodules of this study was vernadite, a nanocrystalline and turbostratic phyllomanganate with hexagonal layer symmetry. In layer growth structures of hydrogenetic origin, Fe-vernadite dominates. Layer growth structures of suboxic-diagenetic origin contain three vernadite forms, which are the main Ni and Cu carriers. These Mn-phases were identified on the basis of their structural layer-to-layer distances (7 Å and 10 Å) and on their

capacity to retain these distances when heated. The first form is 7 Å vernadite, which is minor component of the nodules. The second is a thermally unstable ~10 Å vernadite collapsing between room temperature and 100 °C and the third is a thermally stable ~10 Å vernadite collapsing between 100 and 300°C. Todorokite was neither detected in bulk nodules nor in any of the individual suboxic-diagenetic growth structures. Because the mineralogical composition of the nodule is quite homogeneous (only different vernadite-types), it is suggested that the content of Ni and Cu in the individual growth structures is controlled by their availability in the environment during individual growth phases.

A profile through a CCZ nodule revealed that the thermal stability of the vernadites change from younger (thermally unstable vernadites, collapsing <100 °C) to older growth structures (thermally stable 10 Å vernadites, collapsing > 100 °C) of the nodule accompanied with changes in type and amount of interlayer cations (e.g., Mg, Na, Ca, K). The stability of the vernadites is probably due to re-organization and incorporation of metals within the interlayer of the crystal structure.

Keywords: manganese nodules, phyllomanganates, vernadite, todorokite, HRTEM analysis, cation exchange experiments

Introduction

Manganese nodules forming on the ocean seafloor in water depth between 4000 and 6500 m consist of Mn-Fe (oxy)hydroxides, which contain high amounts of economically important metals such as Ni, Cu, Zn, Co, Mo and rare earth elements (Koschinsky and Halbach 1995; Hudson-Edwards 2000; Takahashi et al. 2007; Hein et al. 2013).

An economically important area for Mn-nodules exploration is located within the Clarion and Clipperton Zone (CCZ) in the central equatorial Pacific. This area has high abundance of Mn-nodules (up to 30 kg/m^2; Rühlemann et al. 2010) that contain high concentration of Ni (1.32 ± 0.21 wt%), Cu (1.21±0.11 wt%), and Co (0.15 ± 0.02 wt%) (data from Wegorzewski and Kuhn 2014; Halbach et al. 1988). These nodules consist of individual genetically different layer growth structures (LGS) such as hydrogenetic and diagenetic, which alternate concentrically around a nucleus (Halbach et al. 1988).

Hydrogenetic LGS form due metal precipitation out of oxic near bottom sea water (Halbach et al. 1988; Koschinsky and Halbach 1995) and oxic sediment pore water (Wegorzewski and Kuhn 2014). Those LGS generally have low Mn/Fe ratios (<3) and low Ni+Cu contents (<1.5 wt% but are enriched in Co (~0.4 wt%; Halbach et al. 1988). In contrast, metal precipitation under suboxic conditions leads to LGS of high Mn/Fe ratios (>10; von Stackelberg 1997). LGS of suboxic-diagenetic origin of nodules from the eastern CCZ are characterized by Ni+Cu contents varying between 0.8 wt% and 6.5 wt%, but these nodules are low in Co (0.07±0.07 wt%; data from Wegorzewski and Kuhn 2014; Halbach et al. 1988).

The individual LGS may consist of different Mn-Fe-oxide minerals. The most common Mn-oxide minerals in those nodules are phyllomanganates, which are built of [MnO_6] octahedral layers, separated from each other by an interlayer space containing hydrated cations. Ordered phyllomanganates with a layer-to-layer distance of ~7 Å (e.g., birnessite) contain one plane of water molecules within the interlayer and 10 Å phyllomanganates (e.g., buserite) contain two planes of water molecules in the interlayer space (Giovanoli et al. 1975; Burns et al. 1977; Golden et al. 1986; Post and Veblen 1990; Drits et al. 1997; Bodeï et al. 2007). These two phyllomanganates have a nano-sized and turbostratic disordered equivalent, termed respectively 7 Å and 10 Å vernadite (Giovanoli et al. 1975; Giovanoli 1980; Manceau et al. 1992; Usui and

Mita 1995; Drits et al. 1997; Villalobos et al. 2003; Manceau et al. 2014). In addition there is a third vernadite variety termed Fe-vernadite (Varentsov et al. 1991).

Turbostratism (Warren 1941) is defined as the systematic occurrence, between adjacent layers that remain parallel, of random rotation of the [MnO_6] octahedral layers around **c*** or of random translation of the [MnO_6] sheets in the **ab**-plane (Giovanoli 1980; Drits and Tchoubar 1990).

X-ray diffraction patterns (XRD) of ordered phyllomanganates (birnessite, buserite) as well as 7 Å and 10 Å vernadites have basal reflections at ~7 Å (001) and ~3.5 Å (002) for the 7 Å varieties and ~10 Å (001) and ~5 Å (002) for the 10 Å varieties, respectively (Bodeï et al. 2007; Drits et al. 2007). At higher diffraction angles disordered phyllomanganates (vernadite) show no *hkl* reflection contrastingly to ordered phyllomanganates (Giovanoli et al. 1975; Drits et al. 1997, 2007; Villalobos et al. 2003; Bodeï et al. 2007), but at least two *hk*-bands (~2.45 Å (10) and ~1.42 Å (11); with band assignment made using $\gamma = 120°$) with the first one being asymmetric (e.g., Drits et al. 2007).

In contrast Fe-vernadite has *hk*-bands at ~2.45 Å (10) and ~1.42 Å (11) (Burns and Burns 1975, 1979; Chukhrov et al. 1979; Golden et al. 1986 Manceau et al. 1992 and references therein) and no (001) reflection because it consists of layers of single edge-shared [MnO_6] octahedra, which are epitaxial intergrown with amorphous δ-FeOOH nanoparticles, which disrupt parallelism between adjacent layers (Burns and Burns 1975).

In general phyllomanganates can have hexagonal or orthogonal layer symmetry (Drits et al. 1997), but in natural samples hexagonal symmetry dominates (Jones and Milne 1956; Post 1992). The octahedral layers of hexagonal phyllomanganates can contain abundant isomorphic substitution of Mn^{4+} (for example by Mn^{3+}) and vacancies, thus inducing layer charge deficit (Burns 1976, Dillard et al. 1982, Manceau et al. 1997; 2002). The negative charge deficit is balanced by hydrated interlayer cations, which form outer-sphere complexes in the middle of the

95 interlayer space (e.g., Na^{+}, Ca^{2+}) or inner-sphere complexes above/below layer vacancies (e.g.,
96 Mn^{2+}; Mn^{3+}, Ni^{2+}, Cu^{2+}, Zn^{2+}, Cr^{2+}; Post and Bish 1988; Manceau et al. 1997, Lanson et al. 2000;
97 Peacock and Sherman 2007a, b; Manceau et al. 2014).
98 Additionally to phyllomanganates, the tectomanganate todorokite is also described to occur in
99 diagenetic Mn-nodules (Burns and Burns 1975, 1978a, b; Burns et al. 1977; Chukhrov et al.
100 1979; Halbach et al. 1988; Manceau et al. 1992, 2007, 2014; Usui and Glasby 1998; Bodeï et al.
101 2007; Drits et al. 2007). Todorokite consist of edge-sharing 3 x 3 [MnO_6] octahedral triple chains
102 forming a 3D tunnel structure (Chukhrov et al. 1979; Turner and Buseck 1979; Turner et al.
103 1982; Post et al. 2003; Bodeï et al. 2007; Atkins et al. 2014). The negative layer charge of
104 todorokite originates from substitution of Mn^{4+} by cations of lower valance (e.g., Mn^{3+}, Ni^{2+}).
105 This fact, in addition to an intrinsically high affinity for many trace elements, explains why
106 phyllomanganates have a higher layer charge and accordingly a higher potential to sorb metals
107 (e.g., Ni up to 5 wt%) than todorokite (Ni $\leq$ 2 wt%; Bodeï et al. 2007).
108 XRD pattern of todorokite have a Bragg peak at ~10 Å, similar to the (001) reflection of 10 Å
109 phyllomanganates, but also has characteristic diffractions peaks in the higher angle region (2.22
110 Å, 1.90 Å, 1.74 Å and 1.54 Å; JCPDS-38-0475; Peacock and Sherman 2007b; Manceau et al.
111 2014). Furthermore, a diffraction peak at around 2.40 Å is observed, even when 10 Å
112 phyllomanganate and todorokite are mixed on a fine scale (Manceau et al. 2014). According to
113 different authors, todorokite in nodules is often a transformation product of Mg-rich buserite
114 during late diagenetic processes or because of hydrothermal influence during nodule growth (e.g.,
115 Bodeï et al. 2007; Atkins et al. 2014; Manceau et al. 2014).
116 The main topic of this paper is, beside the mineralogical characterization of bulk nodules, the
117 detail mineralogical investigation of the nm to µm genetically different LGS in context of the
118 varying Ni+Cu content. The results should provide information about if the mineralogical

119 composition of Mn-oxides controls the incorporation of Ni and Cu into the nodules. Furthermore,
120 detailed mineralogical investigation and understanding of metal association with occurring
121 minerals in Mn-nodules is of prime importance with regard to further efficient metallurgical
122 treatment.
123

124 ## Materials and methods

125 ### Nodule samples

126 The nodules that are presented in this work were collected in the German eastern license area
127 within the CCZ in the central Pacific Ocean during cruise SO205 in 2010 (R/V SONNE;
128 Rühlemann et al. 2010) and cruise BIONOD 2012 (R/V L`Atalante; Rühlemann et al. 2012). The
129 exploration area is located between 119°30`W to 115°`W and 13°N to 11°N at a water depth of
130 4000 – 4500 m (Table 1, Fig. 2 in Wegorzewski and Kuhn 2014). Detailed information about the
131 origin of the nodules can be found in Rühlemann et al. (2010).
132 The analyzed nodules (09KG-B, 26KG, 29KG-C, 32KG-4, 32KG-5, 44KG-2, 62KG-A) are
133 typical for the German eastern license area. They have a spherical to ellipsoidal shape with
134 approximate diameters ranging between 4 and 8 cm. Their upper sides, which were in contact
135 with the near bottom sea water, are smooth and the lower sides that were buried within the upper
136 few cm in the sediment are rough. Bigger nodules show botryoidal growth structures on both
137 sides. All nodules consist of nm – µm thick LGS, which are concentrically arranged around a
138 nucleus (e.g., rock fragments, micro nodules; Halbach et al. 1988). Figure 1 in the supplementary
139 represents a cross section of such a typical Mn-nodule from the German eastern license area
140 within the CCZ.

Mineralogical investigations were carried out on bulk nodules as well as on individual nm – µm thick LGS. For the detail chemical and mineralogical investigation of individual LGS, nodule 32KG-5 (Fig. 1) was chosen because of well formed LGS with high variation of the metal content (Ni+Cu 0.8 – 6.5 wt%; Wegorzewski and Kuhn 2014). In addition, a profile was drilled along a big nodule (44KG-2; 10 x 8 x 8 cm) to investigate chemical and mineralogical changes with age and depth within the nodule (Supplementary Fig. 1).

Analytical methods

X-ray diffraction

The mineralogical composition of several natural bulk nodules was determined using XRD. Drying experiments were conducted at different temperatures to get information about the thermal stability of the Mn-phases. Nodule 26KG was grinded at room temperature (RT) in a first step, without prior drying, and analyzed using XRD. Further XRD analyses of this nodule were conducted after drying at 40 °C, 100 °C and 300 °C for 24 hours each. Sample 32KG-5 was dried at 40 °C, 100 °C, 150 °C, 200 °C and 300 °C. This approach allows to distinguish between todorokite (stable ≥ 300 °C; Bish and Post 1989; Shen et al. 1993; Ching et al. 1999), thermally stable 10 Å phyllomanganates (stable between 100 and < 300 °C), and thermally unstable 10 Å phyllomanganates (collapsing between RT and 100 °C).

Furthermore, several additional nodules (9KG-B; 29KG-C, 32KG-4, 44KG-2, 62KG-A) were analyzed just after drying at 40 °C and 100 °C to investigate if thermally stable and thermally unstable 10 Å phyllomanganates occur, or if diffraction pattern characteristically for todorokite arise.

XRD patterns of bulk nodules were recorded using a PANalytical X'Pert PRO MPD Θ-Θ diffractometer (Cu-Kα radiation generated at 40 kV and 30 mA), equipped with a variable divergence slit (20 mm irradiated length), primary and secondary soller, Scientific X´Celerator detector (active length 0.59°), and a sample changer (sample diameter 28 mm). The samples were investigated as continuous scan at a step size of 0.0167° from 2° to 85° 2Θ with nominal time per step of 10 sec. Specimens were prepared using the top loading technique.

In addition to bulk samples, individual samples (mixture of several nm - µm thick LGS) of a drilled profile through nodule 44KG-2 were analyzed using XRD. The samples were drilled with a high precision planar drill bit (diameter of 6 mm) from nodule surface down to the core (~3 cm). The powder samples were analyzed with a Philips PW-1800 X-ray diffractometer. The apparatus has a graphite diffracted beam monochromator (Cu-Kα) radiation generated at 40 kV and 40 mA equipped with an automatic divergence slit. The samples were investigated from 2° to 80° 2Θ with a step size of 0.02° 2Θ and a counting time of 5 sec per step. All samples were analyzed twice, after drying the sample at 40 °C and at 100 °C for 24 h each.

Inductively coupled plasma optical emission spectrometry

In order to determine the chemical composition of the samples from the drill profile of nodule 44KG-2 (samples correspond to a mix of individual LGS), the samples were dried at 110 °C for 24h. Afterwards the samples were dissolved with $HCl/HNO_3/HF$ in a ratio of 3:1:1 mL. The solutions were diluted to 50 g in 0.5 M HNO_3 and 0.05 M HCl. Major and minor elements (Mn, Fe, Ni, Cu, Co, Al, K, Ca etc.) were analyzed with inductively coupled plasma optical emission spectrometry (ICP-OES; Spectro Ciros Vision). Analytical precision and accuracy were checked by analyses of certified standard materials such as BGR standard FeMn-1 (Kriete 2012), Mn nodule standards NOD-P-1 (United States Geologic Survey) and JMn-1 (Geological Survey of

Japan). For a detailed description of the methodology, accuracy, and precision as well as interference refer to Alexander (2008).

Electron microprobe analysis

Chemical composition of individual growth structures within nodule 32KG-5 (Fig. 1) was investigated using electron microprobe analysis (EMPA; CAMECA SX 100). For the analysis, thick sections (0.2 mm) were prepared. The analyses of genetically different LGS were performed using a 15 and 20 kV accelerating voltage and 40 nA beam current. The bright LGS (Mn-rich) were measured with a focused (1 – 5 μm) beam and the darker LGS (Fe-rich) with a defocused (5 – 20 μm) beam. The counting times for the analyzed elements were 10 s for Mn, Fe, Ni, Cu, Na, Mg, Al, Si, K, Ca, Ti, P, S, Cl, 40 s for V, 45 s for Pb, 50 s for Co, 90 s for Zn, 100 s for Ba, Mo and Sr, and 110 s for Ce. Rhodochrosite (Mn), hematite (Fe), cobaltite (Co), synthetic Ni_2Si (Ni), cuprite (Cu), albite (Na), kaersutite (Mg, Al, Si), biotite (K), apatite (Ca, P), rutile (Ti), willemite (Zn), barite (S, Ba), monazite (Ce), molybdenite (Mo), krokoite (Pb), celestine (Sr), vanadium metal (V) and tugtupite (Cl) were used as standards (BGR standards). A PAP matrix correction was applied to measurements (Pouchou and Pichoir 1991).

The hydrated, very porous Mn oxides that build up the individual LGS of Mn nodules contain a high amount of water (approx. 20%; Hein et al. 2013). Therefore, this material is sensitive to the high beam current causing total analytical sums < 100%. We decided to take total analytical sums of ≥ 80% as acceptable, all analyses <80% were omitted from further investigations.

Focused ion beam and high-resolution transmission electron microscopy

For structural analysis of individual LGS, high-resolution transmission electron microscopy **(**HRTEM) was used. Electron transparent foils from LGS of nodule 32KG-5 were cut using the

Focused ion beam (FIB) preparation technique. Cutting sites from LGS of interest were selected based on EMPA and are marked in Fig. 1. The foils (15 x 10 x 0.15 μm) were sputtered from the target material using Ga-ions with energy of 30 keV (Wirth 2009). For HRTEM analyses, foils were taken out from their excavation sites applying the so-called lift-out technique (Giannuzzi et al. 1997). Detailed description of the FIB techniques is given in Gianuzzi and Stevie (2005) and Wirth (2004; 2009). HRTEM analyses were carried out with a FEI F20 X-Twin transmission electron microscope with Schottky field emitter as an electron source at the GeoForschungs Zentrum Potsdam (GFZ). The HRTEM is equipped with a Gatan Imaging Filter. HRTEM bright-field and dark-field images as well as high-resolution lattice fringe images were acquired as energy filtered images applying a 20 eV window to the zero-loss peak. The HRTEM images were performed at 200 kV. Diffraction pattern were calculated from high-resolution lattice fringe images (using Fast Fourier Transformation). High-angle annular dark field images were acquired using a Fishione system.

Cation exchange experiments

For further differentiation between the two so-called 10 Å manganese minerals todorokite and phyllomanganates, cation exchange experiments **(**CEE) were carried out on different nodules from the CCZ. Powdered samples were filled in centrifuge tubes with 2 mL of 1M KCl solution. After centrifugation, the supernatant was decanted and fresh solution was added. This procedure was performed three times. Thereafter, the samples were transferred to porous ceramic tiles and washed three times with deionized water and analyzed via XRD. The same procedure was subsequently carried out on the same samples with 2 mL of 1M $MgCl_2$ solution.

Results

Mineralogy of bulk nodules

XRD drying experiments

Figure 2 show XRD patterns of a typical CCZ nodule (26KG) after different drying steps (RT, 40 °C, 100 °C, and 300 °C). The XRD pattern of the RT sample shows broad but distinct reflections at 9.9 Å and 4.9 Å which can be attributed to the (001) and (002) reflections of a 10 Å phyllomanganate or to diffraction maxima of todorokite (e.g., Post and Bish 1988; Manceau et al. 2014). Only a small and weak hump around 7 Å can be recognized and is attributed to the (001) reflection of a 7 Å phyllomanganate. After drying the sample at 40 °C the intensity of the reflection at 9.9 Å decreased and that of the maximum at 7 Å increased. After drying at 100 °C, the 10 Å peak was broadened and slightly shifted to higher diffraction angles (~9 Å). After drying at 300 °C the reflections at ≈10 Å and ≈5 Å as well as ≈7 Å disappeared completely. In another nodule sample (32KG-5), the reflections at ≈10 Å and ≈5 Å disappeared almost after drying the sample at 150 °C and is completely collapse after drying at 200°C (Table 2).

All other bulk nodules were analyzed exclusively after drying at 40 °C and 100 °C. Their XRD pattern showed considerable changes upon drying, the initial pattern having an intense diffraction maximum at ≈10 Å (9.7 – 9.9 Å) and a weak diffraction maximum at ≈7 Å (7.1 – 7.4 Å), and the final pattern having a very weak and broad diffraction maximum between 9 to 9.7 Å and a stronger diffraction maximum at ≈7 Å (7.1 – 7.3 Å) as well as two maximum at ≈2.45 Å and ≈1.42 Å (Table 2). The ≈2.45 Å reflection is broad and asymmetrical and the ≈1.42 Å reflection is symmetrical. The ratio of the two values is ~1.73 in all samples.

Finally, quartz (Qz) and minor amounts of phillipsite (Ph) were detected in the nodule samples (Fig. 2).

XRD of profile across nodule 44KG-2

Subsamples from a drilled profile across nodule 44KG-2 (bulk composition in Wegorzewski and Kuhn 2014) were investigated using XRD (Fig. 3). All subsamples, starting at the nodule surface down to ~30 mm (near the core) display after heating at 40 °C (XRD electronic annex 1) broad but distinct reflections at ≈10 Å and weak ones at ≈7 Å. Two *hk*-bands are recognized at ≈2.45 Å (10) and ≈1.42 Å (11). Upon heating to 100 °C, samples from the surface down to 5 mm within the nodule revealed distinct changes in the low angle region (Fig. 3): The ≈10 Å peak disappeared and the peak around ≈7 Å therefore increased.

After drying at 100 °C, samples from 5.2 mm to 6.8 mm drilling depth still exhibit peaks at ≈10 Å but also increased ≈7 Å peaks, both reflections being broad and of quite similar intensity. The reflection around ≈10 Å moved after drying to lower angle regions (9 – 9.6 Å).

In samples from 6.8 mm down to ~30 mm depth within the nodule, the ≈10 Å peak was still present after heating at 100 °C but became broader and changed position to slightly lower diffraction angles (9 – 9.5 Å). The ≈7 Å peak disappeared completely (Fig. 3).

The diffraction patterns overall showed poor diffracted intensity, which is to a large extent related to the nanometric size of the minerals analyzed. Nevertheless, the different changes within the lower and higher angle region, which are characteristic for different Mn-phases (stable and unstable 10 Å phyllomanganates), are distinct and some conclusions about the mineralogical changes from the surface (younger LGS) to the inner laying LGS (older LGS) of the nodule can be drawn, especially with changes in chemical composition through the profile.

Chemical investigation of the profile through nodule 44KG-2

Chemical analysis of the profile through nodule 44KG-2 also reveals changes from the outer surface of the nodule to its center (near core). The Mn/Fe ratio increases from 5.21 ± 0.63 (upper

10 mm) to 10.79 ± 3.62 (down to 32 mm, near core; Supplementary Table 2). The content of Ni+Cu is variable within the whole profile without a distinct trend. In contrast, an increase of Mg, Ba and K accompanied by a decrease of Na and Ca with depth can be observed (Supplementary Table 2 and Fig. 2).

Individual LGS (HRTEM + EMPA)

LGS of low Mn/Fe ratios (LGS type 1)

LGS type 1 appear as relatively dense layers with a slightly columnar growth structures (Fig. 4a, b) of low reflectivity occurring throughout the whole nodule (32KG-5). For a detailed description see Wegorzewski and Kuhn (2014). EMPA of those LGS show Mn/Fe ratio of 1.19 ± 0.17, the Ni+Cu content as well as the Zn concentrations are also low ranging between 0.4 and 1.0 wt% (median 0.6 wt%) and 0.07 – 0.10 wt% (median 0.1 wt%), respectively (Supplementary Table 3). Cobalt concentrations of these LGS range between 0.35 and 0.54 wt% (median 0.4 wt%). According to the chemical composition (Supplementary Table 3) those LGS are of hydrogenetic origin formed under oxic conditions within the marine environment (Halbach et al. 1981).

HRTEM images of LGS of type 1 (not shown) do not show lattice fringes and further selected area electron diffraction (SAED) patterns do not show crystalline phases, suggesting that the sample analyzed was amorphous or cryptocrystalline. This might indicate that Fe-vernadite, which is epitaxially intergrown with an amorphous FeOOH phase, was analyzed. Indeed, this phase has no 00*l* reflections and weak *hk*-bands, which might have been further weakened by a low amount of sample exposed to the beam.

LGS of high Mn/Fe ratios (LGS type 2)

297 LGS of type 2 occur as two different growth structures: dendritic LGS and dense LGS (Fig. 4a –
298 c). Both types of LGS consist of individual, platy crystals varying in size and density forming a
299 porous network (Fig. 4d). In contrast to LGS of type 1, type 2 LGS reveal high Mn/Fe ratios (13
300 – 826; Supplementary Table 3). According to the high Mn/Fe ratios, those LGS are interpreted as
301 suboxic-diagenetic precipitates (e.g., von Stackelberg 1997).
302 For further mineralogical investigation LGS of type 2 are further classified in four subtypes
303 according to their growth structure and their different Ni+Cu content:

304 **Dendritic LGS with high Mn/Fe ratio (LGS 2.1)**

305 EMPA of the dendritic LGS of nodule 32KG-5 (box 3 in Fig. 1 and its high resolution image in
306 Fig. 4a) reveal Mn/Fe ratios ranging between 13 and 57 and Ni+Cu contents of 2 – 3.8 wt% (Fig.
307 5; Supplementary Table 3). This dendritic LGS shows higher alkali metal content (median K +
308 Na: 4.45 wt%) than earth alkali metals (median Mg + Ca + Ba: 3.46 wt%; Supplementary Table
309 3).
310 In the dendritic LGS lattice fringes with distinct *d*-spacing of ≈7 Å as well as of ≈10 Å were
311 observed by HRTEM (similar to Fig. 4e, f; Table 3). The SAED patterns showed distinct
312 diffraction rings around 5 Å (assigned as the (002) reflection of a 10 Å vernadite), 7 Å ((001)
313 reflection of a 7 Å vernadite), 3.5 Å ((002) reflection of a 7 Å vernadite), and weak diffraction
314 rings at ~2.4 Å (10), and ~1.4 Å (11; Fig. 4e, f; Table 3). Note that, in SAED patterns, the 10 Å
315 reflection (corresponding to the (001) reflection of a 10 Å vernadite) is very close to the primary
316 electron beam, making its detection difficult. Consequently, we will rather use the (002)
317 reflection as a proxy for the occurrence of a 10 Å phase.

318 **Dense LGS with high Mn/Fe ratios (LGS 2.2 and 2.3)**

Two dense LGS of high reflectivity were analyzed. LGS type 2.2 occurs at the bottom side of the nodule, directly below the outermost dendritic LGS (box 3 in Fig. 1 and high resolution image in Fig. 4a) and LGS type 2.3 is located near the nodule top side which was recently in contact with the bottom ocean water (box 1 in Fig. 1 and high resolution image in Fig. 4b). Both LGS show Mn/Fe ratios ranging between 41 and 826 but differ in their metal content (e.g., Ni+Cu; Fig. 5). LGS type 2.2 has Ni+Cu contents ranging between 0.8 and 2.7 wt% (median 1.1 wt%; Fig. 5; Supplementary Table 3). In contrast LGS type 2.3 shows much higher Ni+Cu concentrations (3.8 – 5.4 wt%; median 4.6 wt%, Fig. 5; Supplementary Table 3). Both dense LGS have low Co contents (median 0.02 wt%) and quite similar amounts of alkali and earth alkali metals (~3.8 wt%) whereby the Mg content (~1.8 wt%) is lower than the Na content (~2.9 wt%; Supplementary Table 3).

Both dense LGS types show HRTEM images with distinct *d*-spacing lattice fringes of ≈7 Å (Fig. 4f). The SAED patterns also show distinct diffraction rings around 7 Å, 3.5 Å, and weak ones at ~2.4 Å and ~1.4 Å which correspond probably to 7 Å phyllomanganates (Table 3).

In contrast to the dense LGS of low Ni+Cu content (LGS 2.2), the LGS of high Ni+Cu content (LGS type 2.3) have SAED patterns with diffraction rings also around 5 Å (4.8 Å), which were interpreted here as (002) reflection of a 10 Å phyllomanganate.

Additional, both dense LGS show additional lattice fringes with *d*-spacing of ≈5.5 Å which are assumed to be a completely dehydrated phyllomanganate (Post and Veblen 1990; Cygan et al. 2012).

LGS near the core with homogeneous Mn/Fe ratios (LGS 2.4)

LGS of type 2.4 represents the second growth layer around the nucleus of the nodule and has similar optical properties as LGS of type 2.2 and 2.3 (box 2 in Fig. 1 and its high resolution

image in 4c). The Mn/Fe ratios vary between 65 and 183; the Ni+Cu contents are rather homogenous (3.3 – 3.8 wt%, Fig. 5). Similar to all other described LGS of type 2, the Co contents are low (0.04 ± 0.01 wt%; Supplementary Table 3).

The Mg content (median 2.2 wt%) of this LGS is higher than in the other LGS of type 2 (median ≤1.9 wt%) and higher than the Na content, which is the opposite in the other LGS of type 2 (LGS types 2.1 – 2.3; Supplementary Table 3).

The SAED pattern of LGS type 2.4 shows only diffraction rings around ≈5 Å, assumed again to be the (002) refection of 10 Å phyllomanganates. No evidence for the presence of a 7 Å phyllomanganate was found (Table 3).

The SAED patterns of all type 2 LGS of high Mn/Fe ratios reveal weak reflections around ≈2.4 and ≈1.4 Å. Similar to the bulk XRD results these reflections are characteristic for *hk*-bands of phyllomanganates of hexagonal layer symmetry. The absence of these reflections in some regions of the LGS might be explained by the small particle size (nano-range) and the low crystallinity of natural phyllomanganates, both leading to a decrease of the maximum diffracted intensity.

Cation exchange experiments

The CEE were carried out to find out if the interlayer regions of the phyllomanganates of the nodules studied are accessible for cation exchange of K^+ and Mg^{2+} ions (Fig. 6) as described by Golden et al. (1986).

In samples treated with KCl, the peak position of 10 Å phyllomanganate was shifted from ≈10 Å to ≈7 Å. After treating the same samples with $MgCl_2$, the peak position was shifted from ≈7 Å back to ≈10 Å (Fig. 6). This reaction pathway indicates cation exchange ability typical for phyllomanganates, as discussed by Golden et al. (1986). Nodule samples with a higher ability to exchange K^+ and Mg^{2+} ions in their interlayers (inferred from the increase of the intensity of the 7

365 Å reflection after the exchange with K^+; samples: 09KG-B, 29KG-C and 26KG) seem to contain
366 higher proportions of thermally unstable phyllomanganates compared to nodules with lower
367 exchange capacity (62KG-A, 32KG-4, 44KG-2; 32KG-5; Table 2).

368

369 **Discussion**

370 In many publications the tectomanganate todorokite has been suggested to be the major 10 Å Mn-
371 phase of marine ferromanganese nodules from the CCZ, even if a (turbostratic) Mn-oxide with
372 basal X-ray diffraction reflections at ≈10 Å and ≈5 Å has previously been described (e.g.,
373 Halbach et al. 1981; Turner et al. 1982; Calvert and Piper 1984; Mellin and Lei 1993). The
374 detection and the characterization of different Mn-minerals within nodules is difficult because of
375 the nanometer size of studied minerals, of their poor crystallinity, and because the different Mn-
376 minerals are intergrown with each other on a fine scale. Additionally the fibrous to platy habitus
377 of todorokite and phyllomanganates is quite similar (Giovanoli and Arrhenius 1985).
378 Because of that, special methods were used in this study for the differentiation of todorokite and
379 phyllomanganates in bulk nodules from the eastern CCZ, such as heating and cation exchange
380 experiments. HRTEM analyses of suboxic-diagenetic LGS were conducted to get more
381 information about their mineralogy in context with the high variation in Ni and Cu content.

382 **Bulk mineralogy**

383 The dehydration experiments distinctly show collapsing of the 10 Å reflection from bulk nodules
384 of the German eastern license area after drying up to 300 °C (26KG) or even already at 200 °C
385 (32KG-5; Table 2). This is due to the release of interlayer water molecules from the

386 phyllomanganate structure, as discussed in the literature (Wadsley 1950; Mellin and Lei 1993;
387 Shen et al. 1994).
388 Furthermore, the investigated CCZ nodules show variable but distinct potential to exchange
389 cations in their interlayers (Fig. 6). This is an indication for higher cation exchange capacity,
390 which is much higher for phyllomanganates than for todorokite (Crane 1981; Golden et al. 1986;
391 Bish and Post 1989; Cui et al. 2009).
392 These observations together with the absence of typical diffraction peaks for todorokite at lower
393 diffraction angles of the XRD patterns of presently studied nodules (between 2.4 and 1.4 Å;
394 Atkins et al. 2014; Manceau et al. 2014), plead for todorokite being absent from the present
395 samples, or at least below the detection limit. Instead, the major Mn-phase is a thermally stable
396 10 Å phyllomanganate (collapsing between 100 °C and 200 or 300 °C).
397 Further, all XRD patterns (before and after heating steps) show only two *hk*-bands at lower
398 diffraction angles around 2.45 Å and 1.42 Å, whereof the first one is asymmetric. These results
399 indicate that the detected phyllomanganates are turbostratically disordered 10 Å and 7 Å
400 vernadites (Manceau et al. 2014) with a hexagonal symmetry (Drits et al. 1997). This is also in a
401 good agreement with the almost symmetrical shape of the 1.42 Å reflection, which would be split
402 into a double peak in case of orthogonal layer symmetry (Drits et al. 2007). All these information
403 can be quantitatively validated by modeling an X-ray diffraction pattern typical for this kind of
404 nodules (Fig. 7, Supplementary Table 1).
405 At this point it's worth mentioning that there is another stable 10 Å manganate oxide, which can
406 occur in marine manganese nodules such as asbolane (Chukhrov et al. 1982; 1983; Manceau et al.
407 1992), which complicates the characterization of the 10 Å Mn-phase. Using XRD, asbolane can
408 be generally recognized by strong (002) reflection ((002) reflection shows higher intensity than
409 the (001) reflection) and generally a split of the two *hk*-bands (Manceau et al. 1992; Manceau et

al. 2014). According to that as well as to the low Ni+Co/Mn (0.01 – 0.06) we assume that if asbolane is present, it occurs in trace amounts.

However, the dehydration experiments revealed that already at RT some of the 10 Å vernadites dehydrate (Fig. 2). These results further suggest that the 7 Å vernadites after heating at 40 °C and 100 °C are dehydration products of thermal unstable 10 Å vernadites and do not represent original 7 Å vernadites as already suggested by Arrhenius and Tsai (1981), Usui et al. (1989) as well as Mellin and Lei (1993). We interpret the 7 Å vernadite to form only a minor amount within nodules from the German eastern license area.

Samples 09KG-B, 29KG-C and 26KG mainly consist of thermally unstable 10 Å vernadite due to the collapsing of the 10 Å diffraction at <100 °C and with simultaneously higher ability to expand the layer structure and therefore exchange cations in their interlayers (Table 2; Fig. 6). In contrast to that nodules 62KG-A, 32KG-4, 44KG-2 and 32KG-5 consist of thermally stable (collapsing of the 10 Å peak >100 °C) as well as thermally unstable 10 Å vernadite (collapsing <100 °C) in almost equal proportions (Table 2).

The different thermal stability and cation exchange ability is probably due to different amounts and types of cations/metals (e.g., Na^{+}, K^{+}, Ca^{2+}, Mg^{2+}, Ni^{2+}, Cu^{2+}) and their way to be incorporated in the structure (possibly as inner-sphere or as outer-sphere complexes or being incorporated within vacancies of the [MnO_6] octahedra).

Elements which form inner-sphere complexes above layer vacancies (in a triple corner-sharing coordination – TC configuration) share 3 oxygen atoms from layer vacancies, and they are coordinated to other water molecules and/or hydroxyl groups that point towards the interlayer (e.g., $Mn^{2+/3+}$ and metals such as Cu^{2+}; Little et al. 2014; Manceau et al. 2014). Such coordination sphere cannot accommodate a strong layer-to-layer decrease when it faces a similar complex located on the other side of the interlayer, and when the interlayer also contains significant

amounts of alkali (see Manceau et al. 2014, for a detailed discussion). In contrast, when the mineral structure contains little cations sorbed in a TC configuration, but mainly elements forming outer-sphere complexes in the center of the interlayer space (e.g., K^+, Na^+, Ca^{2+}), the interlayer spacing can collapse.

Furthermore, prior dehydration experiments on synthetic phyllomanganates (birnessite like structures) with different cations (e.g., Na^+, Ca^{2+}, Mg^{2+}, Zn^{2+}, Ni^{2+}) in the interlayer (Golden et al. 1986; Mellin and Lei 1993; Johnson and Post 2006) showed that the collapsing is due to the hydration energy of the individual cations. 10 Å phyllomanganates with cations of low hydration energy such as Na^+ (Johnson and Post 2006) collapse already at RT and those with higher hydration energy such as Mg^{2+} do not dehydrate until 300 °C (Golden et al. 1986; Mellin and Lei 1993; Johnson and Post 2006). This would explain why stable and unstable phyllomanganates were detected, and would imply that the stable 10 Å variations are more likely to occur in LGS of high Mg content (as interlayer cations) and higher metal content (forming inner-sphere complexes).

Individual layered growth structures

HRTEM analyses of individual LGS were carried out to investigate the relation between the different Ni+Cu concentrations (0.8 – 5.4 wt%, Supplementary Table 3) and their mineralogy. These details were studied on suboxic-diagenetic LGS of type 2 with variable Ni+Cu contents.

According to the HRTEM analyses in context with the bulk mineralogy, all LGS of type 2 consist of hexagonal 7 Å and 10 Å vernadites, as shown in a recent study of Manceau et al. (2014) that focused on a nodule from the west Pacific Ocean. Those vernadites incorporate trace metals such as Ni and Cu within their [MnO_6] octahedral layers or additionally as inner-sphere complexes above/below the octahedral vacancies in the case of Cu (Peacock and Sherman 2007b; Little et al. 2014; Manceau et al. 2014).

458 In general the LGS of type 2 reveal predominantly 7 Å vernadite when observed with HRTEM.
459 This result seems to be in contrast to the XRD analyses of bulk nodules with 10 Å vernadite
460 being the major Mn-phase. But the two data can be reconciled by assuming that during the
461 HRTEM analysis partial dehydration of the 10 Å vernadite may occur, because of the vacuum
462 conditions applied (Turner and Buseck 1979; Post and Veblen 1990) or because of the sample
463 preparation (drying samples at 40 °C and prior grinding; Usui et al. 1989).
464 HRTEM analysis of dense LGS type 2.2 indicates only 7 Å phyllomanganates. This LGS
465 contains in contrast to all other suboxic-diagenetic LGS of this study (LGS type 2.1, 2.3, and 2.4)
466 the lowest Ni+Cu concentrations. Further, in this LGS the Mg content is lower than the Na
467 content. The combination of these two properties is probably responsible for the sole occurrence
468 of 7 Å vernadites, which probably are the dehydration product of a so-called thermally unstable
469 10 Å vernadite. Further, it could be assumed that the metals such as Ni and Cu are preferably
470 incorporated within the [MnO_6] octahedral layers (e.g., Peacock and Sherman 2007b; Manceau et
471 al. 2014) instead of forming inner-sphere complexes above/below vacancies, which could rather
472 lead to a structure stabilization.
473 In contrast to that, suboxic LGS of type 2.1 and 2.3 indicate the occurrence of both 7 Å as well as
474 10 Å vernadites intergrown with each other on a fine scale when analyzed using HRTEM. The
475 detection of 10 Å vernadites was probably caused by higher Mg and Ni+Cu contents in these two
476 LGS compared to LGS type 2.2. But in both LGS still the content of Mg is lower than Na similar
477 to LGS type 2.2, suggesting Na^+ is the main interlayer cation. It can be suggested that Cu is
478 forming partly inner-sphere complexes above/below vacancies (Little et al. 2014) resulting in
479 formation of more stable 10 Å phyllomanganates and that Ni is completely incorporated within
480 the [MnO_6] octahedral layers (Peacock and Sherman, 2007b; Manceau et al. 2014). According to
481 Peacock and Sherman (2007a, b) and Sherman and Peacock (2010), at circumneutral pH, only

some Ni and Cu will be incorporated within the octahedral layers of phyllomanganates and will be sorbed in a TC configuration above/below vacancy sides at lower pH (pH ≤4; Peacock and Sherman 2007a; Peacock 2009). Further, more stable vernadite phases can have higher amounts of Mn (Mn^{2+}, Mn^{3+}) within the interlayer forming TC complexes above/below the vacancy sites of the [MnO_6] octahedral sheets stabilizing the structure against collapsing. The 7 Å vernadite of these two LGS then can be either an original phase or a collapsed form of a 10 Å vernadite of low metal loading (e.g., Na as interlayer cation and metals such as Ni and Cu incorporated in the octahedra).

In contrast, LGS of type 2.4 shows the highest Mg and lowest Na concentrations within all suboxic LGS with simultaneous high content of Ni and Cu. This may favor the formation of a thermally stable 10 Å Mg-vernadite. The 10 Å vernadite probably will be stabilized due to Mg (high hydration energy) and Cu (plus possibly Mn^{2+} and Mn^{3+}) forming TC complexes above/below the vacancies of [MnO_6] octahedral layers. Already Chukhrov et al. (1979) assumed that different stable phyllomanganate types such as buserite-I and buserite-II within manganese nodules could be present. Buserite-I is a thermal unstable 10 Å phyllomangante because of low amounts of interlayer metals compared to buserite-II, which is a more stable 10 Å phyllomanganate with higher metal loading (Chukhrov et al. 1979). These observations fit very well with the different detected phyllomanganates of this study.

Furthermore, the interpretation of the profile through nodule 44KG-2 analyzed by XRD as well as individual suboxic-diagenetic LGS analyzed by HRTEM reveals a stabilization of the 10 Å vernadite structure with respect to interlayer collapsing from the outer nodule surface into deeper (older) nodule areas. This may indicate post depositional transformation. Inner LGS indeed show no distinct enrichment of metals such as Ni and Cu in contrast to the younger outermost LGS but a distinct enrichment of Mg over Na. The substitution of e.g., Na with Mg as well as a possible

rearrangement of the metal (e.g., Ni, Cu) position (from being incorporated within the octahedra to inner-sphere complexes due to pH changes of the environment) probably leads to the stabilization of the mineral structure. Similar mineral distribution (stable and unstable phyllomanganates) with depth (i.e., age) within a nodule was also observed by Smetannikova et al. (1991).

The occurrence of phyllomanganates as the main Mn-phase (in contrast to todorokite), whatever the metal content, indicate that the mineralogy alone does not control the incorporation of metals into the lattice of the Mn-phases during suboxic-diagenetic growth. The amount of metals is rather dependent on the availability of such metals according to the surrounding environmental conditions such as the redox state, the metal flux into the sediment and the early-diagenetic potential mobilization of the sediments. According to that, manganese nodules can act as a good paleoceanographic archive but as assumed by Peacock (2009) this holds only true if the incorporation of those metals (e.g., Ni and Cu) is irreversible during pH fluctuations. According to the high porosity of Mn-nodules (up to 60%; Halbach et al. 1988) and their pore connectivity through the whole nodule fluids from the surrounded environment can influence Mn-phases and change their chemical composition so that chemical characteristics of especially older LGS may be altered with time. The mobility potential of those metals in Mn-phases of marine nodules with increasing age or changes in environmental conditions (such as pH) is not fully understood and deserves more investigations.

The absence of todorokite

The mineralogical investigations of nodules from the eastern CCZ indicate the absence of todorokite as major Mn-phase in nodules from the eastern German license area within the CCZ. This conclusion is based on four observations.

529 (1) The relatively low Mg contents of these nodules (≤2 wt%; Wegorzewski and Kuhn 2014).
530 According to Bodeï et al. (2007) the Mg concentration in phyllomanganate, which transform to
531 todorokite, ranges between 4.1 and 4.9 wt% (Table 2 in Bodeï et al. 2007). Also Manceau et al.
532 (2014) show increased Mg concentrations up to ~4 wt% in diagenetic nodule material which
533 transformed from vernadite to todorokite. Mg has a hydrated diameter of 8.6 Å, close to that of
534 the 3 x 3 tunnel structure of todorokite (Manceau et al. 2014) and is therefore a favorable
535 template ion (Bodeï et al. 2007; Manceau et al. 2014). However, individual suboxic LGS (LGS
536 type 2) of nodules from this study reveal maximal 2.4 wt% Mg, which is probably too low for a
537 transformation of 10 Å vernadite to todorokite.
538 (2) The transition from 10 Å phyllomanganate (buserite) to tunnel-structure todorokite in
539 synthetic samples generally takes place under hydrothermal treatment (e.g., 155 – 160 °C, Ching
540 et al. 1999; Bodeï et al. 2007). A similar conclusion was drawn by Usui et al. (1989). They
541 interpreted their mineralogical data as two series of manganates: a hydrothermal, todorokite-like
542 series consisting of tunnel structures with low amounts of cations and a buserite-like series
543 consisting of octahedral layers with a high content of stabilizing cations. The CCZ nodules were
544 not influenced by hydrothermal fluids and thus the formation of todorokite cannot be favored.
545 However, Grangeon et al. 2014 could show for the first time that a tectomanganate Mn-phase
546 (cryptomelane) can form from vernadite at RT, but at low pH (~3-4).
547 (3) According to Bodeï et al. (2007), the formation of natural as well as synthetic todorokite starts
548 preferable with a **c**-ordered Mg-rich 10 Å phyllomanganate. The product of the transformation
549 from a turbostratic 10 Å vernadite is a mixture of 7 Å vernadite with jianshuite/Mg-chalcophanite
550 and secondary poorly-crystallized todorokite (Bodeï et al. 2007).
551 (4) Higher amounts of ions such Mn^{3+} and Cu^{2+}, which have a Jahn-Teller distorted coordination
552 sphere, promote the transformation of 10 Å phyllomanganate to todorokite and stabilize

553 todorokite in suboxic marine sediments (Siegel and Turner 1983; Bodeï et al. 2007). Such
554 observation was also made by Grangeon et al. (2014) for the vernadite to cryptomelane
555 transformation. They assumed that such transformation with time is driven by the migration of
556 Mn^{3+} with time from octahedral position to the interlayer, until sufficient interlayer Mn^{3+} in a TC
557 configuration is present to allow forming the walls of the tectomanganate structure. Probably the
558 amount of Mn^{3+}, in vernadites octahedral layers of nodules from the recent study, which would
559 be able to migrate from the octahedral layer to the interlayer with time, is too low for kinking of
560 the [MnO_6] octahedral layers forming a tectomanganate.
561 All these facts support the occurrence of phyllomanganates in nodules from the German eastern
562 license area as major Mn-phases rather than todorokite.

563

564 **Implications**

565 The results of this work reveal that ferromanganese nodules from the German eastern license area
566 of the CCZ consist of thermally differently stable turbostratic phyllomanganates of the vernadite-
567 type of hexagonal symmetry rather than of todorokite.
568 Hydrogenetic LGS (type 1) consist of Fe-vernadite, which is epitaxially intergrown with
569 amorphous FeOOH phase. In contrast to that, suboxic-diagenetic LGS (type 2) consist of three
570 different types of vernadites:
571 **1)** 7 Å vernadites forming a minor component in the nodules, mainly it is a dehydration product
572 of unstable turbostratic 10 Å phyllomanganates already collapsing at room temperature.
573 **2)** Unstable 10 Å vernadite collapsing after drying between 40 °C and 100 °C.
574 **3)** Stable 10 Å vernadite collapsing between 100 °C and 200/300 °C.

575 Based on the results of this study it is assumed that the different vernadite types occur because of
576 different incorporated cations in the interlayer which can form inner-sphere complexes (e.g.,
577 $Mn^{2+/3+}$, Mg^{2+}, Ni^{2+}, Cu^{2+}) or outer-sphere complexes (e.g., Na^{+}, K^{+}). Additionally, metals such
578 as Cu^{2+} or even Ni^{2+} can migrate with time from being incorporated within the octahedral layers
579 out of the octahedra to form inner-sphere complexes about the layer vacancies (depending on the
580 environment pH; Peacock and Sherman 2007a,b; Peacock 2009), which may further influence the
581 thermal stability of the crystal structure of phyllomanganates.
582 The recent work shows, that the different amounts of Ni+Cu (0.8 – 5.4 wt%) of individual
583 suboxic-diagenetic LGS are not due to the presence of different Mn-minerals such as todorokite
584 or phyllomanganate but rather depend on the mobility and enrichment of metals within different
585 environmental conditions.
586 Investigations of older and younger nodule areas furthermore reveal a distinct change of the
587 stability of vernadite. Young areas show more unstable vernadite phases than older ones with
588 both low as well as high Ni+Cu contents. This could be explained by a post-depositional
589 incorporation of Mg^{2+} which substitute for e.g. Na^{+} in the interlayer and/or re-arrangement of
590 metals (or Mn) position in the crystal lattice of the Mn-oxides.
591 Due to the low growth rates (1 to >10 mm 10^{6} $year^{-1}$) Mn-nodules are an important
592 paleoceanographic archive (Frank 2002; Han et al. 2003) to reconstruct the environment
593 conditions during individual growth periods. High Mn/Fe ratios of LGS of type 2 indicate a
594 strong Mn-Fe fractionation as it occurs under suboxic environmental conditions. If the metal
595 content is not depending on the mineralogy, it may be a proxy of the individual metal contents
596 and/or metal mobility of the environment within which the nodule have grown. However, the
597 stabilization of phyllomanganates could represent the pH conditions under which they formed.
598 Mn-phases which form at higher pH conditions (pH 7-8) incorporate Ni and Cu rather in the

599 octahedral layers and are therefore of low thermal stability. Thermally more stable
600 phyllomanganates form probably under lower pH conditions (pH 4), where Ni and Cu build up
601 inner-sphere complexes, as shown by experimental analyses (Peacock and Sherman (2007a, b)
602 and Peacock (2009)). But if the incorporation of metals such as Ni and Cu is depending on the pH
603 conditions and the incorporation is reversible the metal contents may not reflect individual metal
604 concentrations in the environment during individual growth phases (Peacock 2009).
605 At this point we only can speculate why nodules from the eastern license area show
606 phyllomanganates with different thermal stabilities. Further extended X-ray absorption fine
607 structure analyses of individual LGS of these nodules have to be conducted to investigate the
608 local environment of Mn, Ni, Cu and other economical important metals. This task is important
609 for further metallurgical treatment of nodules from the German eastern exploration license area of
610 the CCZ.

611

612 **Acknowledgements**

613 We greatly appreciate the work of the master and his crew on expedition SO205 with R/V Sonne
614 during which the samples for this study were taken.
615 We thank J. Lodziak and C. Wöhrl for an excellent support during the EMP analysis at the
616 Federal Institute for Geosciences and Natural Resources (BGR). Furthermore, we gratefully
617 acknowledge the expert help of D. Weck (BGR) in XRD analysis, N. Schleuning (BGR) for
618 cation exchange experiments as well as A. Schreiber from the German Research centre for
619 geosciences (GFZ) in Potsdam for foil preparation using FIB. Furthermore, we thank F. Simon
620 from the Leibniz Institute of Polymer Research, Dresden for the excellent XPS analyses. This

621 study was financed by the Federal Institute for Geosciences and Natural Resources (BGR,
622 Germany) under the project A-0203002.A.

623

624 **References**

625 Alexander, B.W. (2008) Trace element analyses in geological materials using low resolution
626 inductively coupled plasma mass spectrometry (ICP-MS). Jacobs University Technical Report,
627 18.

628

629 Arrhenius, G., and Tsai, A.G. (1981) Structure, phase transformation and prebiotic catalysis in
630 marine manganite minerals. Scripps institution of Oceanography, Reference Series, 81, 1-19.

631

632 Atkins, A.L, Shaw, S., and Peacock, C.L. (2014) Nucleation and growth of todorokite from
633 birnessite: Implications for trace-metal cycling in marine sediments. Geochimica et
634 Cosmochimica Acta, 144, 109-125.

635

636 Bish, D.L., and Post, J.E. (1989) Thermal behavior of complex, tunnel-structure manganese
637 oxides. American Mineralogist, 74, 177-186.

638

639 Bodeï, S., Manceau, A., Geoffroy, N., Baronnet, A., and Buatier, M. (2007) Formation of
640 todorokite from vernadite in Ni-rich hemipelagic sediments. Geochimica et Cosmochimica Acta,
641 71, 5698-5716.

642

643 Burns, R.G. (1976) The uptake of cobalt into ferromanganese nodules, soils, and synthetic
644 manganese (IV) oxides. Geochimica et Cosmochimica Acta, 40, 95-102.

Burns R.G., and Burns, V. M. (1975) Mechanism for nucleation and growth of manganese nodules. Nature, 255, 130-131.

Burns V.M., and Burns R.G. (1978a) Authigenic todorokite and phillipsite inside deep-sea manganese nodules. American Mineralogist, 63, 827-831.

Burns V.M., and Burns R.G. (1978b) Post-depositional metal enrichment processes inside manganese nodules from the north equatorial Pacific. Earth and Planetary Science Letters, 39, 341-348.

Burns V.M., and Burns R.G. (1979) Manganese oxides. In R.G. Burns, Ed., Marine Minerals, 6, 1-46. Reviews in Mineralogy and Geochemistry, Mineralogical Society of America Chantilly, Virginia.

Burns R.G., Burns, V.M., and Easton A.J. (1977) The mineralogy and crystal chemistry of deep-sea manganese nodules, a polymetallic resource of the twenty-first century. Philosophical Transactions of the Royal Society A, 286, 283-301.

Calvert S.E., and Piper D.Z. (1984) Geochemistry of ferromanganese nodules from DOMES Site A, Northern Equatorial Pacific: Multiple diagenetic metal sources in the deep sea. Geochimica et Cosmochimica Acta, 48, 1913-1928.

Ching, S., Krukowska, K.S., and Suib, S.L. (1999) A new synthetic route to todorokite-type manganese oxides. Inorganica Chimica Acta, 294, 123-132.

669 Chukhrov, F.V., Gorshkov, A. I., Beresovskaya, V.V., and Sivtsov, A.V. (1979) Contributions to
670 the mineralogy of authigenic manganese phases from marine manganese deposits. Mineralium
671 Deposita, 14, 249-261.
672
673 Chukhrov, F.V., Gorshkov, A.I., Vitovskaya, I.V., Drits, V.A., Sivtsov, A.I., and Rudnitskaya,
674 E.S. (1982) Crystallochemical nature of Co-Ni asbolan. Izvestia Akademia Nauk, SSSR, Seriya
675 Geologicheskaya, 6, 73-81. (Translated in International Geological Review, 24, 598-604.
676
677 Chukhrov, F.V., Gorshkov, A.I., Drits, V.A., Shterenberg, A.V., and Sakharov, B.A. (1983)
678 Mixed-layer asbolan-buserite minerals and asbolans in oceanic iron-manganese concretions.
679 International Geology Review, 25, 838-847
680
681 Crane, S.E. (1981) Structural chemistry of the marine manganate minerals and model
682 compounds, Ph. D. thesis, University of California, San Diego.
683
684 Cui, H., Qiu, G., Feng, X., Tan, W., and Liu, F. (2009) Birnessites with different average
685 manganese oxidation states synthesized, characterized, and transformed to todorokite at
686 atmospheric pressure. Clays and Clay Minerals, 57, 715-724.
687
688 Cygan, R.T., Post, J.E, Heaney, P.J., and Kubicki, J.D. (2012) Molecular models of birnessite and
689 related hydrated layered minerals, American Mineralogist, 97, 1505-1514.
690

691 Dillard, J. G., Crowther, D. L., and Murray, J. W. (1982) The oxidation states of cobalt and
692 selected metals in Pacific ferromanganese nodules. Geochimica et Cosmochimica Acta, 46, 755-
693 759.
694
695 Drits, V. A., and Tchoubar, C. (1990) X-ray diffraction by disordered lamellar structures: theory
696 and applications to microdivided silicates and carbons. Springer-Verlag: Berlin, 371 p.
697
698 Drits, V. A., Silvester, E., Gorshkov, A. I., and Manceau, A. (1997) Structure of synthetic
699 monoclinic Na-rich birnessite and hexagonal birnessite: I. Results from X-ray diffraction and
700 selected-area electron diffraction. American Mineralogist, 82, 946-961.
701
702 Drits, V.A., Lanson, B., and Gaillot, A.C. (2007) Birnessite polytype systematics and
703 identification by powder X-ray diffraction. American Mineralogist, 92, 771-788.
704
705 Frank, M. (2002) Radiogenic isotopes: tracers of past ocean circulation and erosional input.
706 Reviews of geophysics, 40, 1-1.
707
708 Giannuzzi, L.A., and Stevie, F.A. (2005) Introductin to Focused Ion Beams: Instrumentation,
709 Theory, Techniques and Practice, Springer, 98 p.
710
711 Giannuzzi, L.A., Drown, J.L., Brown, S.R., Irwin, R.B., and Stevie, F.A. (1997) Focused ion
712 beam milling and micromanipulation lift-out for site-specific cross-section TEM specimen
713 preparation. In R. Anderson, S. Walck, Ed., Proceedings of the Materials Research Society:

714 Workshop on Specimen Preparation for TEM of Materials IV, 480. Materials Research Society,
715 Pittsburgh, PA, 19-27.
716
717 Giovanoli, R. (1980) On natural synthetic manganese nodules. In Geology and Geochemistry of
718 Manganese (eds.I. M. Varentsov and G. Grassellg) Vol. I, pp. 159-202. E. Schweizerbart`sche
719 Verlagsbuchhandlung, Stuttgart.
720
721 Giovanoli, R., and Arrhzenius, G. (1985) Structural chemistry of marine manganese and iron
722 minerals and synthetic model compounds. In P. Halbach, G. Friedrich, and von U. Stackelberg
723 Ed., (1988) The Manganese Nodule Belt of the Pacific Ocean. Geological Environment, Nodule
724 Formation, and Mining Aspects. Ferdinand Enke Verlag, Stuttgart, 20-31.
725
726 Giovanoli, R., Bürki, P., Giuffredi, M., and Stumm, W. (1975) Layer structured manganese
727 oxide-hydroxides. IV. The buserite group: structure stabilisation by transition elements. Chimia,
728 29, 517-520.
729
730 Golden, D.C., Dixon, J.B., and Chen, C.C. (1986) Ion exchange, thermal transformations, and
731 oxidizing properties of birnessite. Clays and Clay Minerals, 34, 511-520.
732 Golden, D.C., Chen, C.C., and Dixon, J.B. (1987) Transformation of birnessite to buserite,
733 todorokite, and manganite under mild hydrothermal treatment. Clays and Clay Minerals, 35, 271-
734 280.
735
736 Grangeon, S., Lanson, B., Lanson, M., and Manceau, A. (2008) Crystal structure of Ni-sorbed
737 synthetic vernadite: a powder X-ray diffraction study. Mineralogical Magazine, 72, 1279-1291.

738 Grangeon, S., Lanson, B., and Lanson, M. (2014) Solid-state transformation of nanocrystalline
739 phyllomanganate into tectomanganate: influence of initial layer and interlayer structure.
740 Structural Science, 70, 828-838.
741
742 Halbach, P., Scherhag, C., Hebisch, U., and Marchig, V. (1981) Geochemical and mineralogical
743 control of different genetic types of deep-sea nodules from the Pacific Ocean. Mineral Deposita,
744 16, 59-84.
745
746 Halbach, P., Friedrich, G., and von Stackelberg, U. (1988) The Manganese Nodule Belt of the
747 Pacific Ocean. Geological Environment, Nodule Formation, and Mining Aspects. Ferdinand
748 Enke Verlag, Stuttgart, 254 p.
749
750 Han, X., Jin, X., Yang, S., Fietzke, J., and Eisenhauer, A. (2003). Rhythmic growth of Pacific
751 ferromanganese nodules and their Milankovitch climatic origin. Earth and Planetary Science
752 Letters, 211, 143-157.
753
754 Hein, J.R, Mizell, K., Koschinsky, A., and Conrad, T.A. (2013) Deep-ocean mineral deposits as a
755 source of critical metals for high- and green-technology applications: Comparison with land-
756 based resources. Ore Geology Reviews 51, 1-14.
757
758 Hudson-Edwards, K.A. (2000) Heavy metal-bearing Mn oxides in river channel and floodplain
759 sediments. In: Environmental mineralogy: microbial interactions, anthropogenic influences,
760 contaminated land and waste management, Mineralogical Society, London, pp. 207–226.
761

762 Johnson, E.A., and Post, J. (2006) Water in the interlayer region of birnessite: Importance in
763 cation exchange and structural stability, American Mineralogist, 91, 609-618.
764
765 Jones, L. H. P., and Milne, A. A. (1956). Birnessite, a new manganese oxide mineral from
766 Aberdeenshire, Scotland. Mineralogical Magazine, 31, 283-288.
767
768 Koschinsky, A., and Halbach, P. (1995) Sequential leaching of marine ferromanganese
769 precipitates: Genetic implications. Geochimica et Cosmochimica Acta, 59, 5113-5132.
770
771 Kriete, C., 2012. An Evaluation of the Inter-Method Discrepancies in Ferromanganese Nodule
772 Proficiency Test GeoPT 23A. Geostandards and Geoanalytical research, 35, No 3, 319-340.
773
774 Lanson, B., Drits, V. A., Silvester, E., and Manceau, A. (2000) Structure of H-exchanged
775 hexagonal birnessite and its mechanism of formation from Na-rich monoclinic buserite at low
776 pH. American Mineralogist, 85, 826-838.
777
778 Little, S.H., Sherman, D.M., Vance, D., and Hein J.R. (2014) Molecular controls on Cu and Zn
779 isotopic fractionation in Fe-Mn crusts. Earth and Planetary Science Letters, 396, 213-222.
780
781 Manceau, A., Gorshkov, A.I., and Drits, V.A. (1992) Structural chemistry of Mn, Fe, Co, and Ni
782 in manganese hydrous oxides: Part II. Information from EXAFS spectroscopy and electron and
783 X-ray diffraction. American Mineralogist, 77, 1144-1157.
784

Manceau, A., Drits, V. A., Silvester, E., Bartoli, C., and Lanson, B. (1997) Structural mechanism of Co^{2+} oxidation by the phyllomanganate buserite. American Mineralogist**,** 82, (11-12), 1150-1175.

Manceau, A., Lanson, B., and Drits, V. A. (2002) Structure of heavy metal sorbed birnessite. Part III: Results from powder and polarized extended X-ray absorption fine structure spectroscopy. Geochimica et Cosmochimica Acta, 66, 2639-2663.

Manceau, A., Lanson, M., and Geoffroy, N. (2007) Natural speciation of Ni, Zn, Ba and As in ferromanganese coatings on quartz using X-ray fluorescence, absorption and diffraction. Geochimica et Cosmochimica Acta, 71, 95-128.

Manceau, A., Lanson, M., and Takahashi, Y. (2014) Mineralogy and crystal chemistry of Mn, Fe, Co, Ni, and Cu in a deep-sea Pacific polymetallic nodule. American Mineralogist, 99, 2068-2083.

McMurdie, H.F. (1944) Microscopic and diffraction studies on dry cells and their raw materials. Transactions of the Electrochemical Society, 89, 313-326.

Mellin, T. A., and Lei, G. (1993) Stabilization of 10Å-manganates by interlayer cations and hydrothermal treatment: Implications for the mineralogy of marine manganese concretions. Marine Geology, 115, 67-83.

Peacock, C.L. (2009) Physiochemical controls on the crystal-chemistry of Ni in birnessite: Genetic implications for ferromanganese precipitates, Geochimica et Cosmochimica Acta, 73, 3568-3578.

Peacock, C.L., and Sherman, D.M. (2007a). Sorption of Ni by birnessite: Equilibrium controls on Ni in seawater. Chemical Geology 238, 94-106.

Peacock, C.L., and Sherman, D.M. (2007b) Crystal-chemistry of Ni in marine ferromanganese crusts and nodules. American Mineralogist, 92, 1087-1092.

Post, J.E. (1992) Crystal structures of manganese oxide minerals. In H.C.W. Skinner, R.W. Fitzpatrick, Ed., Biomineralization Processes: Iron, Manganese. Catena Supplement 21. Catena, Cremlingen-Destedt, Germany, pp. 51-73.

Post, J.E., and Bish, D.L. (1988) Rietveld refinement of the todorokite structure. American Mineralogist, 73, 861-869.

Post, J. E., and Veblen, D. R. (1990) Crystal structure determinations of synthetic sodium, magnesium, and potassium birnessite using TEM and the Rietveld method. American Mineralogist, 75, 477-489.

Post J.E., Heaney P.J., and Hanson J. (2003) Synchrotron X-ray diffraction of the structure and dehydration behavior of todorokite. American Mineralogist, 88, 142-150.

Pouchou, J.L., and Pichoir, F. (1991) Quantitative analysis of homogeneous or stratified microvolumes applying the model "PAP"; In K.F.J. Heinrich and D.E. Newbury Ed. Electron probe quantification. Plenum Press, New York, pp. 31-75

Rühlemann, C., and shipboard scientific party (2010) Cruise Report “MANGAN”, Microbiology, Paleoceanography and Biodiversity in the Manganese Nodule Belt of the Equatorial NE Pacific. Federal Institute for Geosciences and Natural Resources (BGR), Sonne Cruise.

Rühlemann, C., and shipboard scientific party (2012) Cruise Report “BIONOD”, Biodiversity, Geology and Geochemistry of the German and French Licence Areas for the Exploration of Polymetallic Nodules in the Equatorial NE Pacific. Federal Institute for Geosciences and Natural Resources (BGR).

Shen, Y.F., Zerger, R.P., DeGuzman, R.N., Suib, S.L., McCurdy, L., Potter, D.I., and O`Young, C.L. (1993) Manganese oxide octahedral molecular sieves: preparation, characterization, and applications. Science, 260, 511-515.

Shen, Y.F., Suib, S.L., and O´Young, C.L. (1994) Effects of Inorganic Cation Templates on Octahedral Molecular Sieves of Manganese Oxide. American Chemical Society, 116, 11020-11029.

Sherman, D.M., and Peacock, C.L. (2010) Surface complexation of Cu on birnessite (δ-MnO2): Controls on Cu in the deep ocean. Geochimica et Cosmochimica Acta, 74, 6721-6730.

Siegel, M.D. and Turner, S. (1983) Crystalline todorokite associated with biogenic debris in manganese nodules. Science, 219, 172-174.

Smetannikova, O.G., Nndreyev, S.I., Anikeyeva, L.I., Frank-Kamenetsky, V.A., and Suchkov, I.A. (1991) Genetic control of the mineral composition and structure of oceanic-floor ferromanganese deposites. From: Mineral`nyy sostav I structura okeanicheskikh zhelezomargantsevykh obrazovaniy v svyazi s ikh genezisom, Zapiski Vsesoyuznogo Mineralogicheskogo Obschestva, 3, 31-42.

Takahashi, Y., Manceau, A., Geoffroy, N., Marcus, M. A., and Usui, A. (2007) Chemical and structural control of the partitioning of Co, Ce, and Pb in marine ferromanganese oxides. Geochimica et Cosmochimica Acta, 71, 984-1008.

Turner, S., and Buseck, P.R. (1979) Manganese oxide tunnel structures and their intergrowths. Science, 203, 456-458.

Turner, S., Siegel, M. D., and Buseck, P. R. (1982) Structural features of todorokite intergrowths in manganese nodules. Nature, 296, 841-842.

Uspenskaya, T.Y., Gorshkov, A.I., and Sivtsov, A.A. (1987) Mineralogy and internal structure of Fe-Mn nodules from the Clarion-Clipperton fracture zone. Internal Geology Review, 29, 363-371.

878 Usui, A., and Glasby, G.P. (1998) Submarine hydrothermal manganese deposits in the Izu-Bonin-
879 Mariana arc: an overview. Island Arc, 7, 422-431.
880
881 Usui, A., and Mita, N. (1995) Geochemistry and mineralogy of a modern buserite deposit from a
882 hot spring in Hokkaido, Japan. Clays and Clay Minerals, 43, 116-127.
883
884 Usui, A., Mellin, T. A., Nohara, M., and Yuasa, M. (1989) Structural stability of marine 10 Å
885 manganates from the Ogasawara (Bonin) Arc: Implication for low-temperature hydrothermal
886 activity. Marine Geology, 86, 41-56.
887
888 Varentsov, I. M., Drits, V. A., Gorshkov, A. I., Sivtsov, A. V., and Sakharov, B. A. (1991) Mn-
889 Fe oxyhydroxide crusts from Krylov Seamount (eastern Atlantic): Mineralogy, geochemistry and
890 genesis. Marine Geology, 96, 53-70.
891
892 Villalobos M., Toner B., Bargar J., and Sposito G. (2003) Characterization of the manganese
893 oxide produced by *Pseudomonas putida* strain MnB1. Geochimica et Cosmochimica Acta, 67,
894 2649-2662.
895
896 Villalobos M., Lanson B., Manceau A., Toner B., and Sposito, G. (2006) Structural model for the
897 biogenic Mn oxide produced by *Pseudomonas putida*. American Mineralogist, 91, 489-502.
898
899 Von Stackelberg, U. (1997) Growth history of manganese nodules and crusts of the Peru Basin.
900 In K. Nicholson, J.R. Hein, B. Bühn and X. Dasgupta, Ed., Manganese Mineralization:

Geochemistry and Mineralogy of Terrestrial and Marine Deposits. Special Publication Geological Society of London, 119, pp. 153-176.

Wadsley, A.D. (1950) A hydrous manganese oxide with exchange properties. Journal of the American Chemical Society, 72, 1782-1784.

Warren, B.E. (1941) X-ray diffraction in random layer lattices. Physical Review, 59, 693-698.

Webb, S.M., Tebo, B.M., and Bargar, J.R., (2005) Structural characterization of biogenic Mn oxides produced in seawater by the marine *bacillus sp.* strain SG-1. American Mineralogist, 90, 1342-1357.

Wegorzewski, A.V., and Kuhn, T. (2014) The influence of suboxic diagenesis on the formation of Manganese nodules in the Clarion Clipperton nodule belt of the Pacific Ocean. Marine Geology, 357, 123-138.

Wirth, R. (2004) Focused Ion Beam (FIB): a novel technology for advanced application of micro- and nanoanalysis in geosciences and applied mineralogy. European Journal Mineralogy, 16, 863-876.

Wirth, R. (2009) Focused Ion Beam (FIB) combined with SEM and TEM: Advanced analytical tools for studies of chemical composition, microstructure and crystal structure in geomaterials on a nanometre scale. Chemical Geology, 261, 217-229.

Figure captions

FIGURE 1 Overview of the thick section of nodule SO205-32KG-5 with marked areas (white boxes) of high-resolution chemical and mineralogical analyses.

FIGURE 2 XRD patterns of a typical CCZ nodule (26KG) after drying at different temperatures (RT = room temperature, 40 °C, 100 °C, 300 °C). Basal reflections of ≈10 Å and ≈7 Å of nodule 26KG change between all drying steps, an increase of the ≈7 Å and a simultaneous decrease of the ≈10 Å peaks represent thermally different stable and unstable turbostratically disordered phyllomanganates with a hexagonal layer symmetry (*hk*-bands at ~2.45 and ~1.42 Å; $d_{10/11}$ = ~1.73). The basal reflections of this CCZ nodule disappeared upon drying at 300 °C.

FIGURE 3 Three characteristic XRD patterns (after drying at 100 °C) of different depth intervals (0 – 30 mm) within nodule SO205-44KG-2. Samples from 0 – 5mm reveal only one basal peak at ≈7 Å, in samples from 5.2 – 6.8 mm two peaks at ≈10 Å and ≈7 Å occur, and in the lower interval only the 10 Å peak is present. This shift indicates the presence of only thermally stable 10 Å phyllomanganates in the lower (older) part of the nodule, and a transition zone with both thermally stable and unstable 10 Å phyllomanganates and only thermally unstable ones close to the surface (youngest part). Stars indicate impurities. Two *hk*-bands at ~2.45 Å and ~1.42 Å can be distinguished.

FIGURE 4 (a) Three different layer growth structures (LGS) at the bottom side of nodule SO205-32KG-5 (marked as area 3 in Fig. 1). Dendritic growth structures (LGS type 2.1), dense layer growth structures (LGS type 2.2) and hydrogenetic layer growth structures (LGS type 1) are shown. **(b)** Representing dense LGS type 2.3 and LGS type 1 (marked as area 1 in Fig. 1). **(c)**

949 LGS type 2.4 near the core of nodule 32KG-5 (marked as area 2 in Fig. 1). **(d)** HAADF image
950 displaying internal growth structure of dense LGS type 2.2 with very thin platy crystals forming a
951 fluffy network. **(e)** HRTEM image: Distinct 10 Å lattice fringes can be distinguished which
952 correspond to 10 Å phyllomanganate and represent the *d*-spacing between two [MnO_6] octahedral
953 layers; insert the corresponding selected area electron diffraction (SAED) image. **(f)** HRTEM
954 image and insert the corresponding SAED pattern of dense LGS type 2.2 in **(a)** representing 7 Å
955 lattice fringes.
956
957 **FIGURE 5** Mn/Fe versus Ni+Cu content of individual layer growth structures (LGS) of type 2 of
958 nodule SO205-32KG-5. All individual LGS have high Mn/Fe ratios and show high variation of
959 the Ni+Cu content.
960
961 **FIGURE 6** XRD patterns of (**a)** sample 29KG-C and (**b)** sample 62KG-A after cation exchange
962 experiments with KCl and MgCl solutions. Blue: original sample without treatment; green: after
963 KCl treatment, red: after MgCl treatment. Note the significant changes in **(a)**.
964
965 **FIGURE 7** Experimental XRD pattern from a typical nodule from German eastern license area
966 of the CCZ (black solid line) and calculated patterns of a turbostratic vernadite (red solid line)
967 and of a birnessite (blue solid line) have the same structure as the vernadite, but 1H stacking
968 mode (i.e. no random stacking fault). In the birnessite pattern (i.e. ordered variation), *hkl* Bragg
969 peaks are expressed, but not observed in the experimental pattern. In the vernadite (i.e.
970 turbostratic variation) pattern, only 00*l* Bragg reflections and asymmetric *hk*-bands are expressed,
971 as in the experimental pattern. The experimental pattern is thus, indexed using the vernadite
972 structure model. Stars indicate impurities. Inset: detailed view of the 3 Å to 1.4 Å region.

973 **Table captions**

974 **TABLE 1** Location of samples analyzed during this study.

975

976 **TABLE 2** Results of XRD analyses of bulk nodules after different heating steps. Symbol +
977 indicates the occurrence and the intensity of the diffraction peaks (+ low intensity, +++ high
978 intensity).

979

980 **TABLE 3** Summarized are the observed *d*-lattice spacings from HRTEM images and the
981 corresponding electron diffraction pattern of individual layer growth structures (LGS) of nodule
982 32KG-5. Symbol x indicates the occurrence of individual lattice fringes and the detectable
983 reflections within selected area electron diffraction pattern of individual LGS.

984

985 **Supplementary**

986 **Figures**

987 **S1** Typical big ellipsoidal nodule (SO205 44KG-2; 10 x 10 x 6.7 cm) with botryoidal grow
988 structures on all sides of the nodule. The top side of the nodule, which was in contact with the
989 near-bottom water is smooth and the bottom side, which was stacking in the upper few cm of the
990 sediment, is rough.

991

992 **S2** The distribution of Mg and Na along a profile through nodule 44KG-2. In the outer parts Na is
993 enriched over Mg, whereas in the inner parts of the nodule Mg is enriched compared to Na.

994

995

Tables

S1 Parameters for the modeling of X-ray diffraction pattern of vernadite typical for nodules of this study.

S2 Chemical composition of the profile trough nodule 44KG-2 (ICP-OES data; wt%)

S3 Average content of major and minor elements of individual LGS types 1 and 2 of nodule 32KG-5 from the CCZ (EMPA data, wt%)

Electronic annes 1

XRD patterns (after drying at 40 °C) of subsamples from different depth intervals (0 – 30 mm) of the profile through nodule SO205-44KG-2. All three pattern indicate distinctly basal peaks at ≈10 Å and broad and low in intensity at ≈7 Å as well as two *hk*-bands at ≈2.45 Å and ≈1.42 Å. Stars indicate impurities.

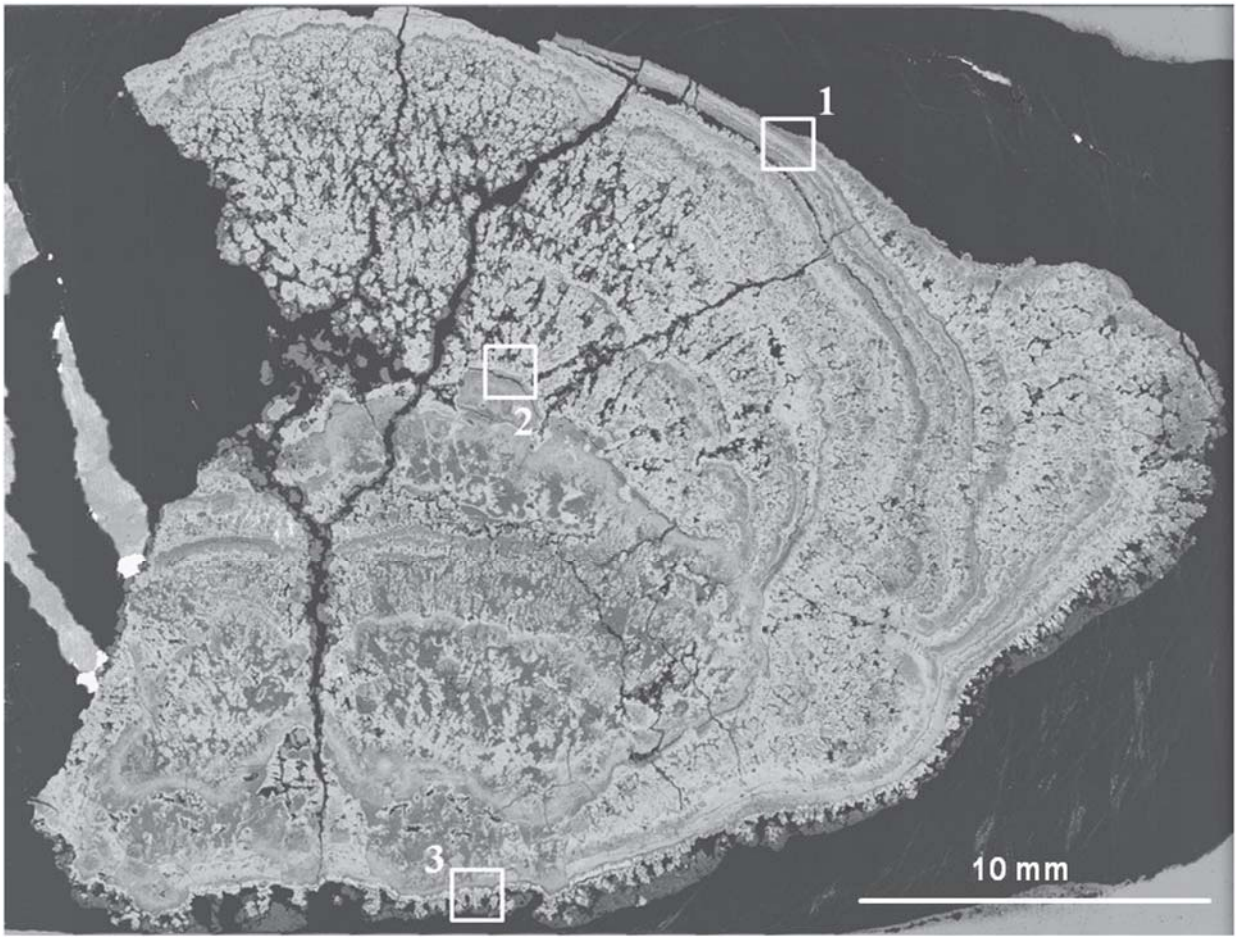
1
2
3
10 mm

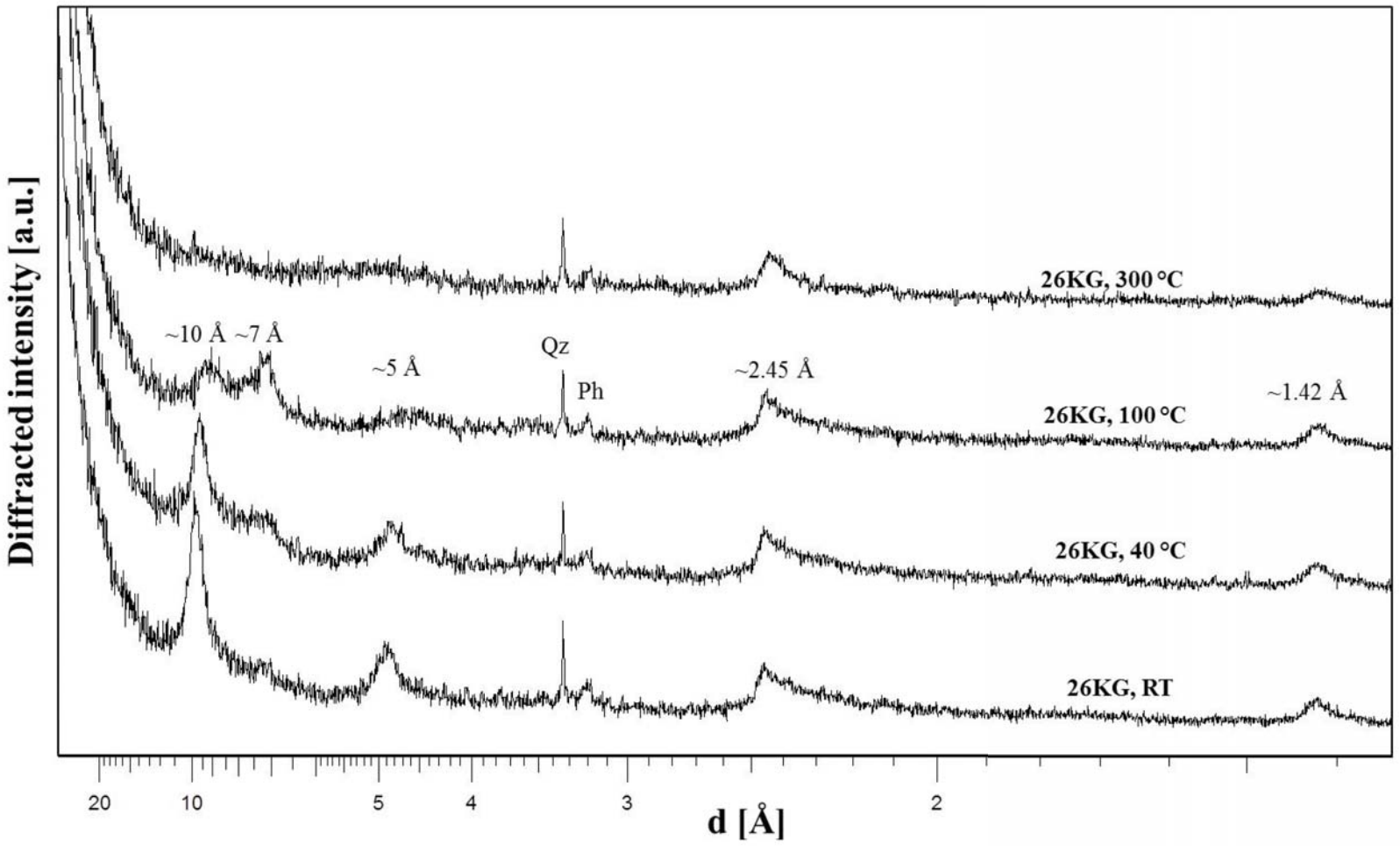
Diffracted intensity [a.u.]
26KG, 300 °C
~10 Å
~7 Å
~5 Å
Qz
Ph
~2.45 Å
~1.42 Å
26KG, 100 °C
26KG, 40 °C
26KG, RT
20
10
5
4
3
2
d [Å]

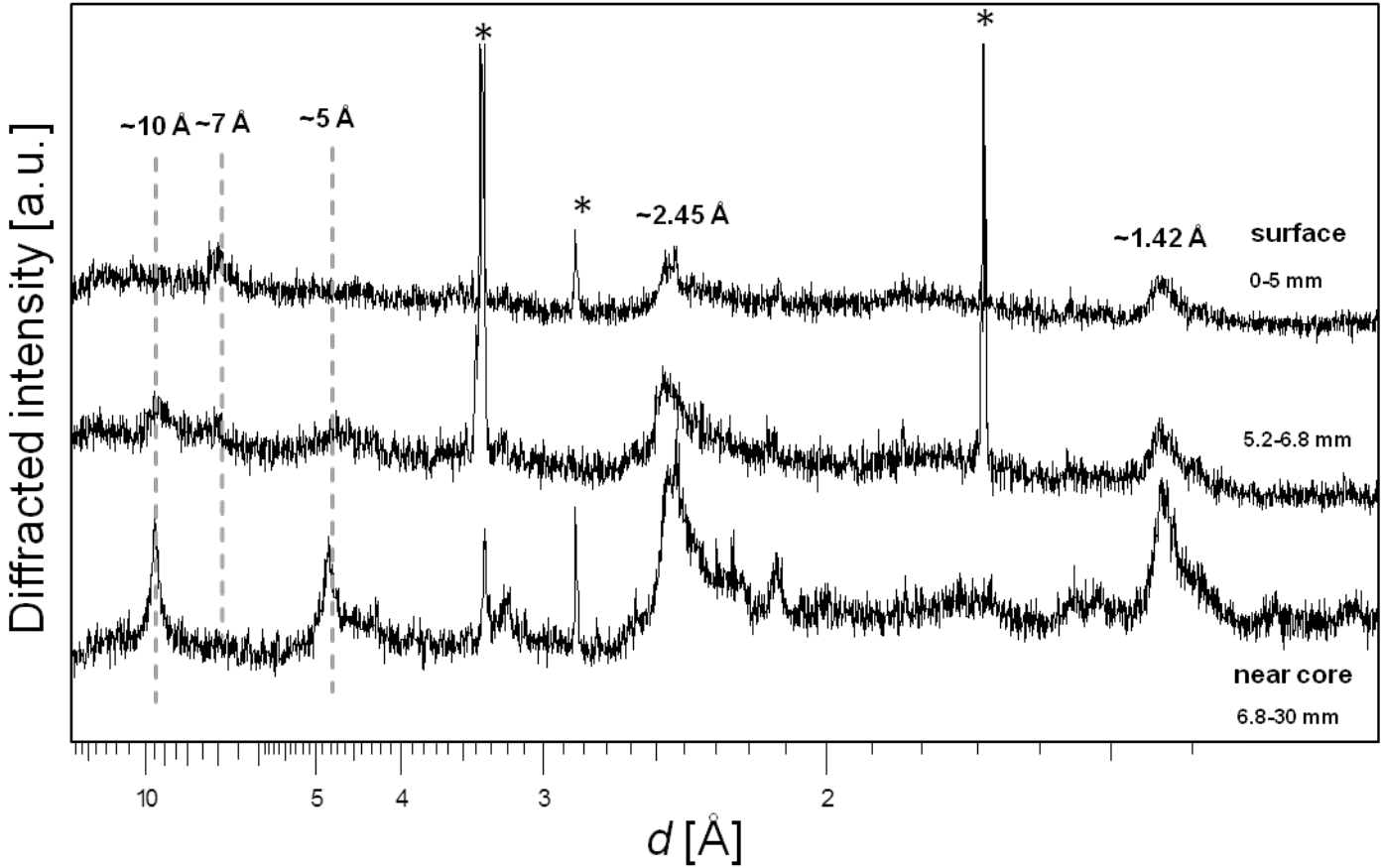
Diffracted intensity [a.u.]
~10 Å
~7 Å
~5 Å
*
*
*
~2.45 Å
~1.42 Å
surface
0-5 mm
5.2-6.8 mm
near core
6.8-30 mm
10
5
4
3
2
d [Å]

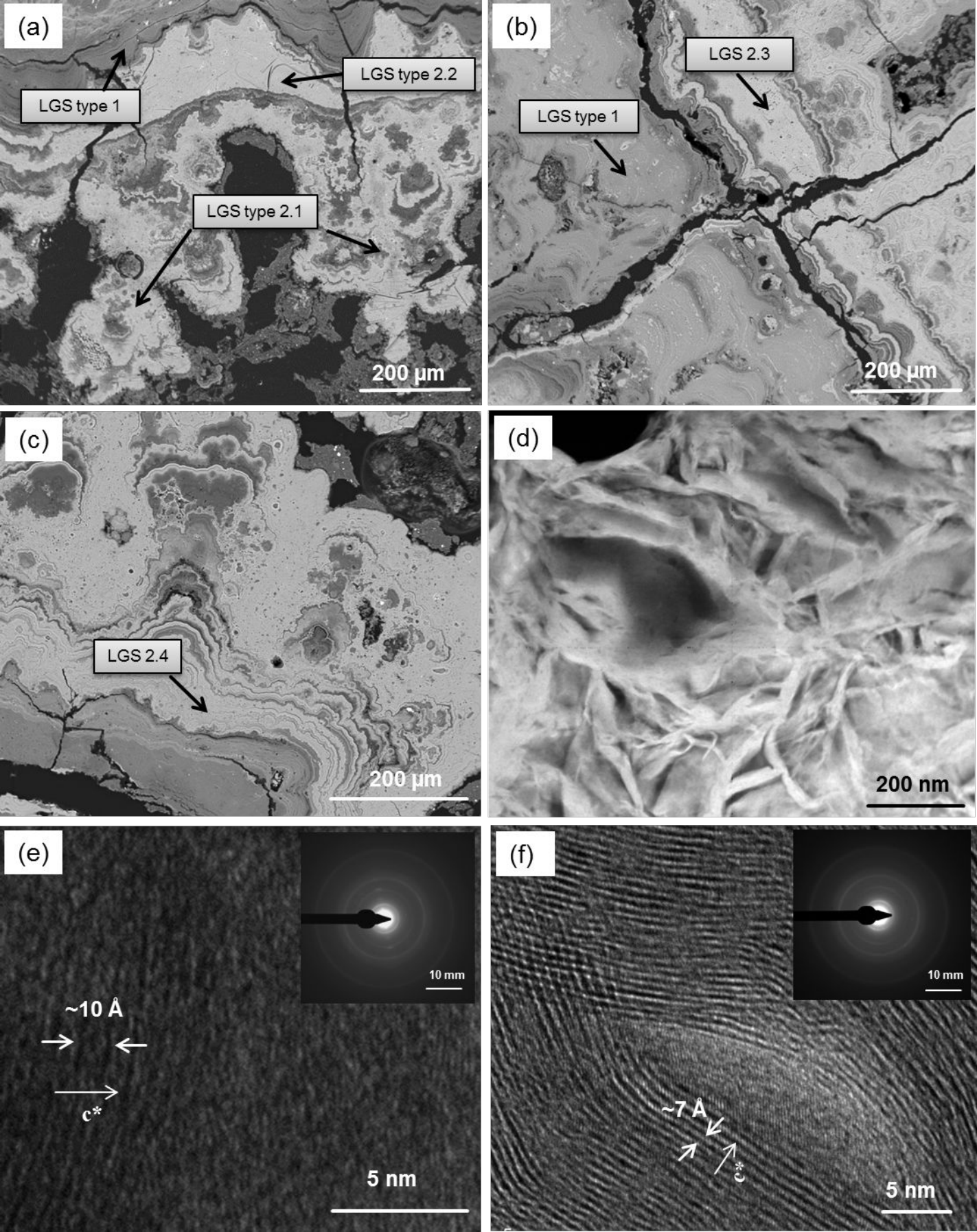
(a)
LGS type 1
LGS type 2.2
LGS type 2.1
200 µm
(b)
LGS 2.3
LGS type 1
200 µm
(c)
LGS 2.4
200 µm
(d)
200 nm
(e)
10 mm
~10 Å
c*
5 nm
(f)
10 mm
~7 Å
c*
5 nm

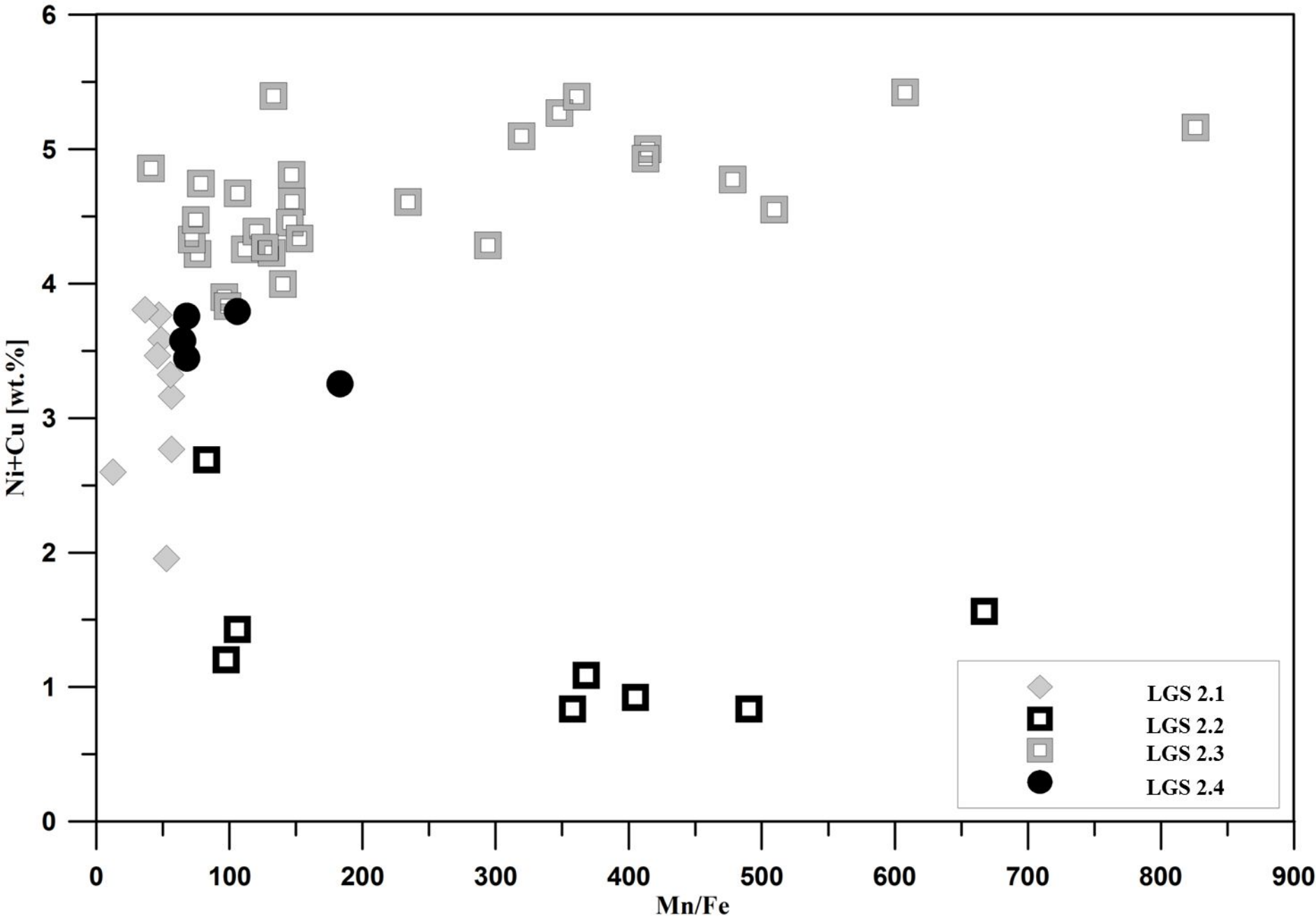
Ni+Cu [wt.%]
Mn/Fe
0
1
2
3
4
5
6
0
100
200
300
400
500
600
700
800
900
LGS 2.1
LGS 2.2
LGS 2.3
LGS 2.4

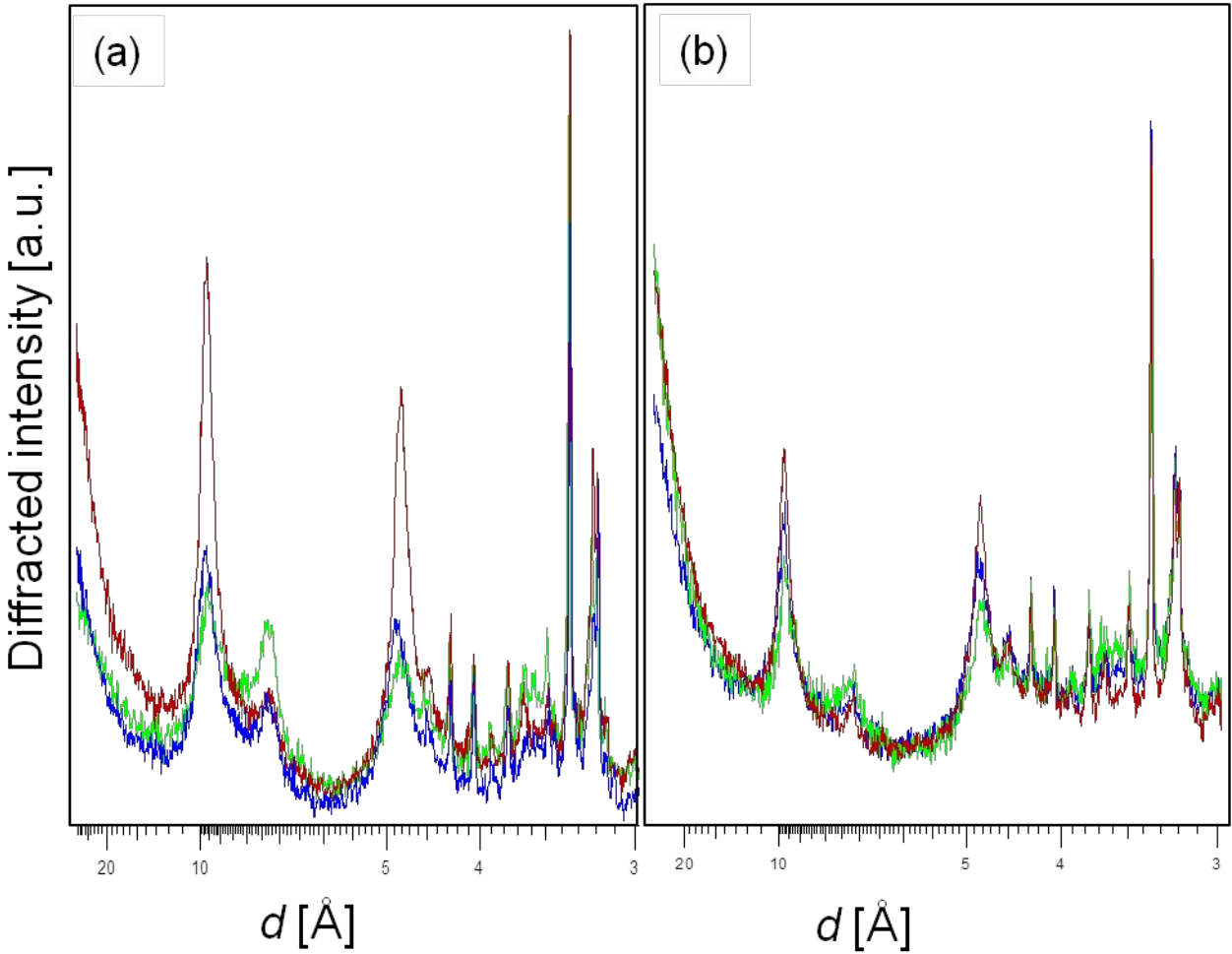
(a)
(b)
Diffracted intensity [a.u.]
20
10
5
4
3
d [Å]
20
10
5
4
3
d [Å]

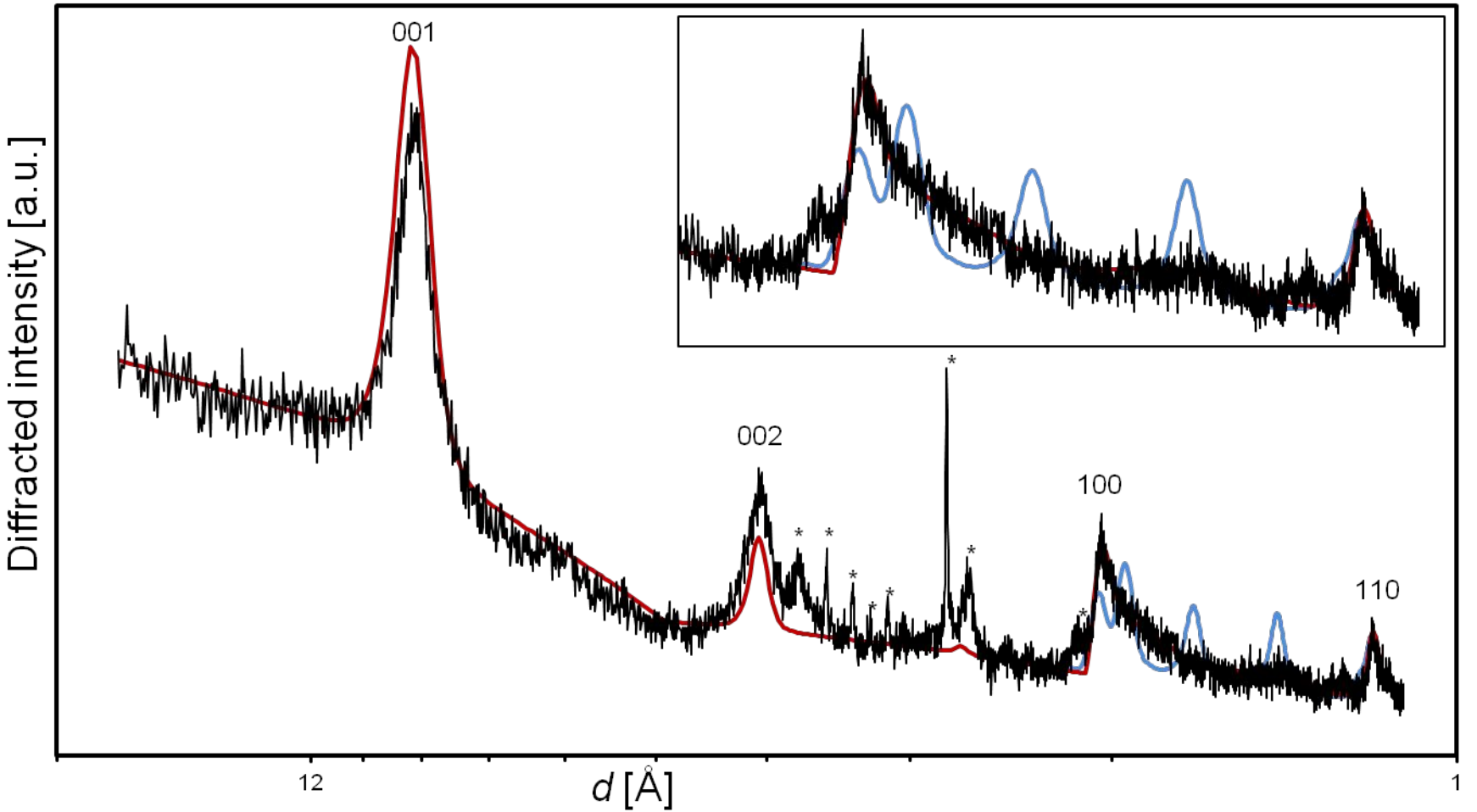
001
002
100
110
*
Diffracted intensity [a.u.]
12
d [Å]
1

TABLE 1 Location of samples analyzed during this study.

Study area (SA)	Sample-ID	Position		Water depth [m]	Water depth [m]
		Latitude	Longitude		
1	SO205 09 KG-B	11°18.6 N	119°14.8 W	4303	midsized discoidal nodule wit smooth surface and rough bottom side
3	SO205 29KG-C	11°35.4 N	116°14.1 W	4203	large discoidal nodule, smooth surface and rough bottom side
	SO205 32KG-4	11°28.6 N	116°9.2 W	4240	midsized nodule with smooth surface and rough bottom side
	SO205 32KG-5	11°28.6 N	116°9.2 W	4240	midsized nodule with smooth surface and rough bottom side
5	SO205 44KG-2	11°57.4 N	116°57.2 W	4188	large nodule, botryoidal growth structures on both sides with a smooth surface and rough bottom side
	BIONOD 26KG	11°53.4 N	117°4.4 W	4137	large discoidal nodule
6	SO205 62 KG-A	13°10.5 N	118°6.3 W	4282	midsized nodule

TABLE 2 Results of XRD analyses of bulk nodules after different heating steps. Symbol x indicates the occurrence and the intensity of the diffraction peaks

sample SO205	RT		40°C		100°C		150°C		200°C		300°C		400°C		500°C	
	10 Å	7 Å	10 Å	7 Å	10 Å	7 Å	10 Å	7 Å	10 Å	7 Å	10 Å	7 Å	10 Å	7 Å	10 Å	7 Å
09KG-B	n.a.	n.a.	+++	+	+	++	n.a.	n.a.	n.a.	n.a.	n.a.	n.a.	n.a.	n.a.	n.a.	n.a.
29KG-C	n.a.	n.a.	++	+	hump	++	n.a.	n.a.	n.a.	n.a.	n.a.	n.a.	–	–	–	–
26KG	+++	hump	++	+	+	++	n.a.	n.a.	n.a.	n.a.	–	–	n.a.	n.a.	n.a.	n.a.
32KG-4[*1]	n.a.	n.a.	++	+	+	+	n.a.	n.a.	n.a.	n.a.	n.a.	n.a.	n.a.	n.a.	n.a.	n.a.
32KG-5	n.a.	n.a.	++	+	+	+	a.d.	a.d.	–	–	–	–	n.a.	n.a.	n.a.	n.a.
44KG-2[*1]	n.a.	n.a.	+++	+	++	++	n.a.	n.a.	n.a.	n.a.	n.a.	n.a.	–	–	–	–
62KG-A	n.a.	n.a.	++	hump	++	++	n.a.	n.a.	n.a.	n.a.	n.a.	n.a.	–	–	–	–

*[1] = analyzed in Wegorzewski and Kuhn (2014), n.a. = not analyzed, - = diffraction peaks disappear; a.g. = almost disappeared

TABLE 3 Summarized are the observed *d*-lattice spacings from HRTEM images and the corresponding electron diffraction pattern of individual layer growth structures (LGS) of nodule 32KG-5. Symbol x indicates the occurrence of individual lattice fringes and the detectable reflections within selected area electron diffraction pattern of individual LGS.

individual layers	layer description	10 Å (001) (HRTEM)	10 Å (001) (SAED)	5.5 Å (001) (HRTEM)	5.5 Å (001) (SAED)	5 Å (002) (SAED)	7 Å (001) (HRTEM)	7 Å (001) (SAED)	3.5 Å (002) (SAED)	2.4 Å (SAED)	1.4 Å (SAED)
layer type 1	dense layer of low reflectivity	-	-	-		-	-	-	-	-	-
layer type 2.1	dendritic structure of high reflectivity	x	-	-	-	x	x	x	x	x	x
layer type 2.2	dense layer of high reflectivity, low Ni+Cu	-	-	x	x	-	x	x	x	x	x
layer type 2.3	dense layer of high reflectivity, high Ni+Cu	-	-	x	-	x	x	x	x	x	x
layer type 2.4	material of high reflectivity, near core	n.a.	-	-	-	x	-	-	-	-	x

n.a. = not analyzed